J. Fluid Mech. (2021), *vol*. 926, A15, doi:10.1017/jfm.2021.710

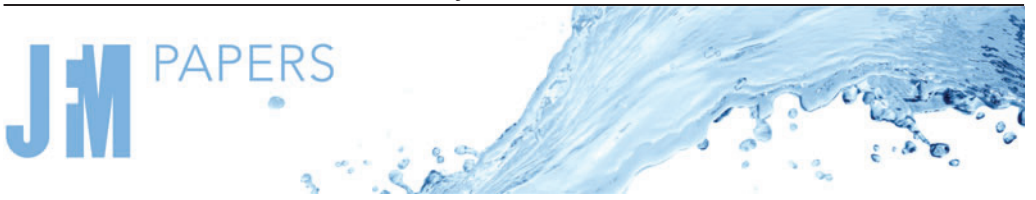

Transition to chaos in a two-sided collapsible channel flow

Qiuxiang Huang[1], **Fang-Bao Tian**[1],†, **John Young**[1] **and Joseph C.S. Lai**[1]

[1]School of Engineering and Information Technology, University of New South Wales, Canberra, ACT 2600, Australia

(Received 11 January 2021; revised 7 June 2021; accepted 4 August 2021)

The nonlinear dynamics of a two-sided collapsible channel flow is investigated by using an immersed boundary-lattice Boltzmann method. The stability of the hydrodynamic flow and collapsible channel walls is examined over a wide range of Reynolds numbers Re, structure-to-fluid mass ratios M and external pressures P_e. Based on extensive simulations, we first characterise the chaotic behaviours of the collapsible channel flow and explore possible routes to chaos. We then explore the physical mechanisms responsible for the onset of self-excited oscillations. Nonlinear and rich dynamic behaviours of the collapsible system are discovered. Specifically, the system experiences a supercritical Hopf bifurcation leading to a period-1 limit cycle oscillation. The existence of chaotic behaviours of the collapsible channel walls is confirmed by a positive dominant Lyapunov exponent and a chaotic attractor in the velocity-displacement phase portrait of the mid-point of the collapsible channel wall. Chaos in the system can be reached via period-doubling and quasi-periodic bifurcations. It is also found that symmetry breaking is not a prerequisite for the onset of self-excited oscillations. However, symmetry breaking induced by mass ratio and external pressure may lead to a chaotic state. Unbalanced transmural pressure, wall inertia and shear layer instabilities in the vorticity waves contribute to the onset of self-excited oscillations of the collapsible system. The period-doubling, quasi-periodic and chaotic oscillations are closely associated with vortex pairing and merging of adjacent vortices, and interactions between the vortices on the upper and lower walls downstream of the throat.

Key words: flow–vessel interactions, blood flow

1. Introduction

Fluid–structure interaction (FSI) problems of collapsible tubes produce rich physiologically significant phenomena in many biological systems (Hazel & Heil 2003; Grotberg &

† Email addresses for correspondence: f.tian@adfa.edu.au; onetfbao@gmail.com

Jensen 2004; Heil & Hazel 2011). For example, the airway of the respiratory system may experience flow-induced instabilities when the deformed airway limits the air being expelled from the lungs. A significant collapse of the upper airway can lead to an obstruction that induces sleep apnoea and flow-induced instabilities that generate snoring noises. Blood vessels may collapse and experience self-excited oscillations as part of their biological function or due to dysfunction. The coronary arteries can be compressed by the surrounding muscular wall of the heart as the heart contracts, and significant collapse may occur (Guiot *et al.* 1990). The brachial arteries will collapse during blood-pressure measurements and generate 'Korotkoff sounds' due to flow-induced instabilities (Bertram, Raymond & Butcher 1989). Leg veins could collapse when subjected to muscular compression to pump blood against gravity up to the heart during exercise, or therapeutic compression for the treatment of deep-vein thrombosis (Dai, Gertler & Kamm 1999).

Though flow-induced vibrations of collapsible vessels are ubiquitous and important in many biological systems, it remains a challenge to study the flow-induced vibrations of collapsible vessels due to nonlinear FSIs involving large deformations, three-dimensional motion, unsteady flows and low-Reynolds-number turbulence (Jensen & Heil 2003). A simplified and classical bench-top experimental model to study the collapsible system is the Starling resistor, in which the flow is driven through a segment of an elastic tube, mounted between two rigid tubes and contained in a pressure-adjustable chamber (e.g. Bertram, Raymond & Pedley 1990, 1991; Bertram & Tscherry 2006). Self-excited oscillations are frequently observed in experiments, and the physical mechanisms for the onset of such oscillations have attracted great interest from the research community. A variety of simplified theoretical and numerical models have been developed to study the self-excited oscillations in the Starling resistor, dating back to lumped-parameter models and one-dimensional (1-D) models (Shapiro 1977; Jensen 1990) and a two-dimensional (2-D) theoretical model introduced by Pedley (1992). A 2-D 'fluid-membrane model' was numerically investigated by Luo & Pedley (1995, 1996), followed by Bernoulli-Euler or Timoshenko 'fluid-beam models' (Cai & Luo 2003; Luo *et al.* 2007, 2008; Liu *et al.* 2009; Liu, Luo & Cai 2012; Tang *et al.* 2015). Such studies have also been extended to three-dimensional (3-D) modelling (Hazel & Heil 2003; Marzo, Luo & Bertram 2005; Heil & Boyle 2010; Zhang, Luo & Cai 2018), which is useful for providing direct comparisons with experiments (Bertram *et al.* 1990; Wang, Chew & Low 2009). Three-dimensional FSI modelling based on experimental data is more helpful in understanding the complex flow mechanisms for the self-excited oscillations of this system. That said, it is believed that 1-D and 2-D models can exhibit most important flow features of this dynamic system with much lower computational costs.

Studies have shown that 1-D models are able to capture some key flow features, including flow separation and wave propagation (Cancelli & Pedley 1985; Jensen 1990). However, the 1-D models are unable to quantitatively agree with experiments or capture the unsteady flow separation.

A simplified 2-D model, first proposed by Pedley (1992) to simulate the Starling resistor, is the flow through an asymmetric collapsible channel (one-sided collapsible channel, as shown in figure 1*a*). Studies of a 2-D fluid-membrane model where the fluid and solid solvers are fully coupled indicate that self-excited oscillations can occur at sufficiently high Re (e.g. 100–500) or sufficiently low membrane tension (e.g. dimensionless tension $T < 6.5$ for $Re = 300$) (Luo & Pedley 1996). Flow separation downstream of the narrowest point and propagating waves possibly generated by the membrane oscillation are also observed. Meanwhile, Luo & Pedley (1996) found that most energy is dissipated in the viscous boundary layers on the upstream elastic channel wall of the indentation. By introducing wall inertia in the 2-D fluid-membrane model, Luo & Pedley (1998) found

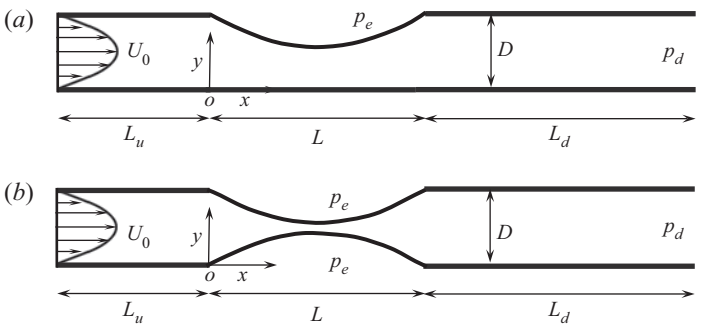

Figure 1. Schematic diagram of fluid flow through collapsible channels. (*a*) One-sided collapsible channel model. (*b*) Two-sided collapsible channel model.

an additional high-frequency flutter mode. Jensen & Heil (2003) studied a pressure-driven asymmetric collapsible channel flow at large tension (dimensionless initial longitudinal tension $T = 10^3 - 10^5$) and moderate Reynolds number flows ($Re = 300 - 500$) by using asymptotic analysis and numerical computation. They found that high-frequency self-excited oscillations occur when the kinetic energy extracted from the mean flow exceeds that dissipated by viscosity. Luo *et al.* (2008) used a combination of a linearized eigenvalue approach and full unsteady numerical simulations to explore the physical mechanisms of large-amplitude self-excited oscillations in a flow-driven asymmetric collapsible channel. A cascade of instabilities was discovered as the wall stiffness was reduced in the wall stiffness-*Re* space. They further demonstrated that the large-amplitude self-excited oscillations consist of mode 2 and higher modes (modes 3 to 4) and the onset of such oscillations is initiated by the linear instabilities of the system (here mode *i* means that the perturbation to the elastic channel wall contains *i* half-wavelengths). Furthermore, small-amplitude flow-induced vibrations of a modulated base flow between two infinitely long compliant walls have also been extensively studied (Lucey & Carpenter 1992, 1995; Davies & Carpenter 1997*a*,*b*; Tsigklifis & Lucey 2017). These studies have revealed various possible modes of instabilities such as Tollmien–Schlichting waves, flow-induced wall-based travelling-wave flutter, divergence instability and modal interactions.

Previous research is mainly focused on one-sided collapsible channels at $Re <= 650$ (Luo & Pedley 1996; Jensen & Heil 2003; Luo *et al.* 2007, 2008; Stewart *et al.* 2010; Tang *et al.* 2015). The biological systems, such as the airway of the respiratory system and blood vessels, are 3-D tubes which can be more reasonably modelled with two-sided collapsible channels, as shown in figure 1(*b*). In addition, as an important application, the typical Reynolds numbers of blood flow range from much less than 1 in venules and capillaries, to 1 in small arterioles to as high as 4000 in large arteries (Ku 1997). The current challenge of the theoretical studies is to extend the combined approach of asymptotics and numerical simulations into flow regimes in the Starling resistor and its physiological applications (Jensen & Heil 2003). Therefore, modelling two-sided collapsible channel flows for a wider range of Reynolds numbers would be more relevant to the real physiological phenomenon and enable comparisons with measurements made in the Starling resistor. While the wall inertia has been neglected in many studies due to the low structure-to-fluid mass ratio in arteries (Jensen 1990; Pedley 1992; Luo & Pedley 1995; Shapiro 1977; Luo *et al.* 2007, 2008; Liu *et al.* 2009; Stewart *et al.* 2010), it may have a significant effect on the stability of this collapsible system even for small values. For some biological systems, the wall inertia is not negligibly small, for example, for airways (e.g. in expiratory wheezing or

the generation of speech) or a diseased blood vessel with intimal hyperplasia. Therefore, here we investigate two-sided collapsible channel flows at higher Reynolds numbers (up to 3000) and a range of mass ratios from 0.3 to 100.

The flow-induced collapse of a flexible tube is a highly nonlinear system. Specifically, Bertram (1986) found that the self-excited oscillations in a thick-walled silicone rubber collapsible tube are highly nonlinear and appear in four discrete frequency bands: 2.7 Hz, 3.8 Hz, 12–16 Hz and 60–63 Hz. Bertram *et al.* (1991) analysed their experimental data by using dynamical system methods and indicated the possible presence of chaotic oscillations. Unfortunately, chaos could not be accurately identified because of the limited lengths of recordings made in the experiments. Jensen (1992) numerically studied 1-D model of unsteady flow in a collapsible tube and demonstrated that the nonlinear interaction between different modes gives rise to quasi-periodic and aperiodic (i.e. irregular or non-repetitive) oscillations. The dependence of the long-time wall motions on the error tolerance level was found as evidence for chaos in the numerical study of a one-sided collapsible channel flow of Luo & Pedley (1996).

Routes to chaos generally include period-doubling bifurcations (Feigenbaum 1978, 1979), quasi-periodic bifurcations (Ruelle & Takens 1971; Newhouse, Ruelle & Takens 1978) and intermittency (Manneville & Pomeau 1980; Miozzi, Querzoli & Romano 1998). The routes of transition from laminar to chaotic motion of collapsible channel flow play an important role in understanding the instability mechanisms in such a system. Zhang, Liu & Lu (2009) conducted a nonlinear dynamic analysis of fluid flow past an inclined flat plate and revealed that the chaotic flow regime could be reached by period-doubling bifurcations and incommensurate bifurcations. Goza, Colonius & Sader (2018) conducted a nonlinear analysis of a flapping inverted flag and characterised the chaotic flapping regime. Kheiri (2020) investigated the nonlinear dynamics of a flexible pipe conveying fluid and identified a quasi-periodicity route to chaos. Still, there is no study on the route to chaos in a collapsible channel flow which is of crucial importance to gain a full understanding of the flow physics in a collapsible channel flow. This is the motivation for this work.

In this work the complex FSI of a two-sided collapsible channel flow is studied by using an immersed boundary-lattice Boltzmann method (IB-LBM). We extend the one-sided collapsible wall channel flow (figure 1*a*) to a two-sided collapsible wall channel (figure 1*b*) with flow regimes more relevant to the Starling resistor and its physiological applications.

The IB-LBM is a relatively new FSI method, which has high capability in modelling large-deformation FSI and remarkable scalability for parallel processing. Feng & Michaelides (2004) first proposed the IB-LBM in simulating rigid moving particles. After that, the IB-LBM has been successfully extended to modelling elastic moving boundaries (Sui *et al.* 2008; Tian *et al.* 2010, 2011*a*,*b*; Krüger, Varnik & Raabe 2011; Zhu *et al.* 2011; Favier, Revell & Pinelli 2014; Hua, Zhu & Lu 2014; Wang & Tian 2018; Xu *et al.* 2018; Feng *et al.* 2019).

The remainder of this paper is organized as follows. In § 2 the 2-D model formulation and governing parameters are described. The numerical method is given in § 3. Numerical results by varying the Reynolds number, structure-to-fluid mass ratio and external pressure are presented in § 4. Finally, conclusions are given in § 5.

2. Model description

We consider a 2-D incompressible flow in a collapsible channel. A segment of the channel wall is replaced by an elastic beam as illustrated by figure 1. The elastic beam has length L and is subjected to an external pressure p_e. The width of the rigid channel is D. A steady

Poiseuille flow with average velocity U_0 is imposed at the initial flow filed, and a constant pressure p_d is specified at the downstream outlet.

The governing equations for the incompressible fluid flow are

$$\nabla \cdot \boldsymbol{u} = 0, \tag{2.1}$$

$$\frac{\partial \boldsymbol{u}}{\partial t} + \boldsymbol{u} \cdot \nabla \boldsymbol{u} = -\frac{1}{\rho_0}\nabla p + \nu \nabla^2 \boldsymbol{u} + \boldsymbol{f}, \tag{2.2}$$

where $\boldsymbol{u}$ is the fluid velocity, ρ_0 is the fluid density, p is the pressure, ν is the kinematic viscosity and $\boldsymbol{f}$ is the body force.

The nonlinear dynamics of the elastic wall is described by Connell & Yue (2007), Huang, Shin & Sung (2007) and Tang *et al.* (2015),

$$\rho_s \frac{\partial^2 \boldsymbol{X}}{\partial t^2} = \frac{\partial}{\partial s}\left[T(s)\frac{\partial \boldsymbol{X}}{\partial s}\right] - EI\frac{\partial^4 \boldsymbol{X}}{\partial s^4} + \boldsymbol{F}, \tag{2.3}$$

where s is the arc length along the elastic wall, $\boldsymbol{X}$ is the position vector of the elastic wall, ρ_s is the linear density of the elastic wall, $T(s)$ is the longitudinal tension, EI is the bending stiffness (where E is the Young's modulus, $I = h^3/12$ is the moment of inertia of the wall cross-section and h is the wall thickness), and $\boldsymbol{F}$ is the force exerted by the fluid and the external pressure.

The averaged flow velocity at the inlet U_0, channel width D, fluid density ρ_0 are used to non-dimensionalize this system, giving five non-dimensional parameters governing this FSI system: the Reynolds number (Re), the structure-to-fluid mass ratio (M), the stretching stiffness (K_s), the bending stiffness (K_b) and the external pressure (P_e),

$$Re = \frac{U_0 D}{\nu}, \quad M = \frac{\rho_s}{\rho_0 D}, \quad K_s = \frac{Eh}{\rho_0 U_0^2 D}, \quad K_b = \frac{EI}{\rho_0 U_0^2 D^3}, \quad P_e = \frac{p_e - p_d}{\rho_0 U_0^2}. \tag{2.4a–e}$$

A no-slip boundary condition is applied along the channel walls, including the elastic segment. The elastic walls are flat initially, and they are clamped at the upstream and downstream rigid walls. Following previous studies of the one-sided collapsible channel flow (Luo *et al.* 2008; Liu *et al.* 2009; Tang *et al.* 2015), the lengths of the upstream and downstream rigid parts of the channel are set as $L_u = 5D$ and $L_d = 30D$, and the length of the elastic wall is $L = 5D$. $K_b/K_s = (h^2/12D^2) \approx 10^{-5}$ for a wall thickness h of 1 % of the channel height.

3. Numerical method

The coupled nonlinear system is solved by using an IB-LBM FSI solver. The numerical algorithm consists of three main parts: the fluid solver, the structure solver and the coupling of fluid and structure dynamics. We adopt the D2Q9 lattice Boltzmann method (LBM) with a multi-relaxation-time (MRT) model for the fluid dynamics. The structural equation (i.e. (2.3)) is solved by the finite difference method, according to Huang *et al.* (2007). The immersed boundary method (IBM) is adopted for the fluid and structural coupling.

3.1. *Lattice Boltzmann method*

The LBM is an alternative and promising numerical scheme for fluid flow simulations due to its advantages of simplicity, explicit calculation and intrinsic parallel nature (Chen & Doolen 1998; Aidun & Clausen 2010; Krüger *et al.* 2017). In the MRT-based LBM,

the fluid state is updated by solving the discrete Boltzmann equation with an MRT collision operator (Lallemand & Luo 2000; Luo *et al.* 2011),

$$g_i(\boldsymbol{x}+\boldsymbol{e}_i\Delta t, t+\Delta t) - g_i(\boldsymbol{x}, t) = \Omega_i(\boldsymbol{x}, t) + \Delta t G_i, \tag{3.1}$$

where $g_i(\boldsymbol{x}, t)$ is the distribution function for particles with velocity $\boldsymbol{e}_i$ at position $\boldsymbol{x}$ and time t. It can be taken as a special probability density function of particles in the Boltzmann equation, but with finite discrete phase spaces and the corresponding collision function (Aidun & Clausen 2010; Krüger *et al.* 2017). Here Δt is the time increment, $\Omega_i(\boldsymbol{x}, t)$ is the collision operator and G_i is the forcing term accounting for the body force $\boldsymbol{f}$. The D2Q9 model is used on a square lattice, of which the discrete velocity components can be represented as

$$\left.\begin{aligned} &\boldsymbol{e_0} = (0, 0), \\ &\boldsymbol{e_i} = (\cos[\pi(i-1)/2], \sin[\pi(i-1)/2])\Delta x/\Delta t, \; i = 1-4, \\ &\boldsymbol{e_i} = \sqrt{2}(\cos[\pi(i-9/2)/2], \sin[\pi(i-9/2)/2])\Delta x/\Delta t, \; i = 5-8, \end{aligned}\right\} \tag{3.2}$$

where Δx is the lattice spacing.

The collision operator $\Omega_i(\boldsymbol{x}, t)$ in the D2Q9 model is derived by Lallemand & Luo (2000),

$$\Omega_i = -(\boldsymbol{M}^{-1}\boldsymbol{S}\boldsymbol{M})_{ij}[g_i(\boldsymbol{x}, t) - g_i^{eq}(\boldsymbol{x}, t)], \tag{3.3}$$

where $\boldsymbol{M}$ is a 9×9 transform matrix for the D2Q9 model and $\boldsymbol{S} = diag(\tau_0, \tau_1, \ldots, \tau_8)^{-1}$ is a non-negative diagonal relaxation matrix. The determination of $\boldsymbol{S}$ can be found in Luo *et al.* (2011). The equilibrium distribution function g_i^{eq} is defined as

$$g_i^{eq} = \rho\omega_i\left[1 + \frac{\boldsymbol{e_i}\cdot\boldsymbol{u}}{c_s^2} + \frac{\boldsymbol{uu}:(\boldsymbol{e_i e_i} - c_s^2\boldsymbol{I})}{2c_s^4}\right], \tag{3.4}$$

where $c_s = \Delta x/(\sqrt{3}\Delta t)$ is the speed of sound, $\boldsymbol{I}$ is the unit tensor, and the weighting factors ω_i are given by $\omega_0 = 4/9$, $\omega_{1-4} = 1/9$ and $\omega_{5-8} = 1/36$. The velocity $\boldsymbol{u}$, density ρ and pressure p can be obtained according to

$$\rho = \sum_i g_i, \quad p = \rho c_s^2 + p_{ref}, \quad \boldsymbol{u} = \left(\sum_i \boldsymbol{e}_i g_i + \frac{1}{2}\boldsymbol{f}\Delta t\right)\Big/\rho, \tag{3.5a–c}$$

where p_{ref} is the reference pressure and $\rho = \rho_0$ at the outlet of the channel. The force scheme proposed by Guo, Zheng & Shi (2002) is adopted to determine G_i,

$$G_i = [\boldsymbol{M}^{-1}(\boldsymbol{I} - \boldsymbol{S}/2)\boldsymbol{M}]_{ij}F_i, \tag{3.6}$$

$$F_i = \left(1 - \frac{1}{2\tau}\right)\omega_i\left[\frac{\boldsymbol{e_i}-\boldsymbol{u}}{c_s^2} + \frac{\boldsymbol{e}\cdot\boldsymbol{u}}{c_s^4}\boldsymbol{e_i}\right]\cdot\boldsymbol{f}, \tag{3.7}$$

where τ is the non-dimensional relaxation time.

3.2. *Immersed boundary method for FSI*

The IBM, first developed by Peskin (1972) to model blood flow in the heart, has been extended to many variants owing to its versatility in handling complex geometries and arbitrarily large deformations (Peskin 2002; Mittal & Iaccarino 2005; Sotiropoulos & Yang

2014; Huang & Tian 2019; Griffith & Patankar 2020). In numerical practice, when fluid flows over a solid body it feels the presence of this body through the forces of pressure and shear force (if the surface of the body is no-slip) along the body surface. Peskin's idea (Peskin 2002) was to represent the immersed solid boundary by applying local body forces in the Navier–Stokes equations. In the IBM the body force $\boldsymbol{f}$ is added in the Navier–Stokes equation to mimic a boundary condition according to,

$$\boldsymbol{f}(\boldsymbol{x}, t) = -\int \boldsymbol{F}_{ib}(s, t)\delta(\boldsymbol{x} - \boldsymbol{X}(s, t))\,\mathrm{d}s, \tag{3.8}$$

$$\boldsymbol{F}_{ib}(s, t) = \alpha\rho(\boldsymbol{x}, t)(\boldsymbol{U}_{ib}(s, t) - \boldsymbol{U}(s, t)), \tag{3.9}$$

$$\boldsymbol{U}_{ib}(s, t) = \int \boldsymbol{u}(x, t)\delta(\boldsymbol{x} - \boldsymbol{X}(s, t))\,\mathrm{d}\boldsymbol{x}, \tag{3.10}$$

where $\boldsymbol{F}_{ib}(s, t)$ is the Lagrangian force density, ds is the arc length of the immersed boundary, $\delta(\boldsymbol{x} - \boldsymbol{X}(s, t))$ is the Dirac delta function, $\boldsymbol{x}$ is the coordinate of the fluid lattice nodes, α is the feedback coefficient and $\alpha = 2s$ in LBM simulations. In dimensionless form $\alpha^* = \alpha/(U_0/D) = 40$, and α^* ranges from 20 to 104. Extensive testing simulations have been conducted to ensure $\alpha = 2s$ is large enough to provide accurate simulations but small enough for numerical stability. Here $\boldsymbol{U}_{ib}(s, t)$ is the immersed boundary velocity obtained by interpolation at the immersed boundary, and $\boldsymbol{U}(s, t)$ represents the velocity of the walls.

The following discrete delta function $\delta_h(\boldsymbol{x})$ is used to approximate the Dirac delta function (Peskin 2002),

$$\delta_h(\boldsymbol{x}) = \frac{1}{\Delta x \Delta y}\phi\left(\frac{x}{\Delta x}\right)\phi\left(\frac{y}{\Delta y}\right), \tag{3.11}$$

$$\phi(r) = \begin{cases} \dfrac{1}{8}\left(3 - 2|r| + \sqrt{1 + 4|r| - 4r^2}\right), & 0 \le |r| \le 1, \\ \dfrac{1}{8}\left(5 - 2|r| + \sqrt{-7 + 12|r| - 4r^2}\right), & 1 \le |r| \le 2, \\ 0, & |r| > 2. \end{cases} \tag{3.12}$$

In this study an iterative feedback IBM (Kang & Hassan 2011) is adopted to handle the interactions between the elastic walls and the fluid. Note that this iterative IBM does not show significant advantages for external flows, but does bring benefits in terms of reducing velocity slip on the walls and enhancing the mass conservation for confined flows.

3.3. *Fluid-solid interface boundary conditions*

Figure 2 shows the schematic of the IB-LBM used in the present solver. The fluid domain is discretized by a fixed uniform Cartesian grid (e.g. Eulerian point $\boldsymbol{x}$), and the immersed boundary is represented by a set of Lagrangian marker points $\boldsymbol{X}^s_{ib}(s = 1, 2, \ldots, N)$. The solid mesh size is half of the lattice spacing. The red shaded area shows the extent of interface where the transfer of forcing $\boldsymbol{F}_{ib}(s, t)$ from Lagrangian boundary point $\boldsymbol{X}(s, t)$ to surrounding fluid nodes and the velocity interpolation for $\boldsymbol{U}_{ib}(s, t)$ from the surrounding fluid nodes.

The Lagrangian force density $\boldsymbol{F}_{ib}(s, t)$ in (3.9) reflects the interaction between the fluid and the structure. It is approximately equivalent to the stress jump at the fluid–structure

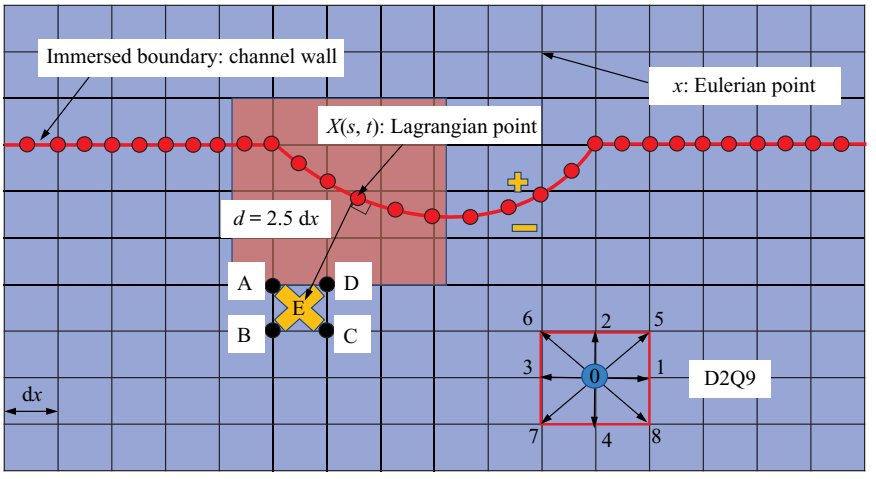

Figure 2. Schematic of the IB-LBM used in the present solver. Red shaded area shows the extent of interface where the transfer of forcing $\boldsymbol{F}_{ib}(s,t)$ from Lagrangian boundary point $\boldsymbol{X}(s,t)$ to surrounding fluid nodes and the velocity interpolation for $\boldsymbol{U}_{ib}(s,t)$ from the surrounding fluid nodes. Here '+' and '−' denote the outward and inward side of the immersed boundary, respectively. The fluid stress at the Lagrangian point $\boldsymbol{X}(s,t)$ is evaluated at 2.5 grid points ($d = 2.5\mathrm{d}x$) inward of the moving boundary (i.e. at lattice E). The letters A, B, C and D are four Eulerian grid points of the lattice E. The fluid stress at the lattice E is evaluated by the inverse distance weighting of the fluid stress at A, B, C and D.

interface, i.e. (Williams, Fauci & Gaver III 2009; Gilmanov, Le & Sotiropoulos 2015)

$$\boldsymbol{F}_{ib}(s,t) \approx -(\sigma^{+} - \sigma^{-}) \cdot \boldsymbol{n}, \tag{3.13}$$

where $\sigma = -p\boldsymbol{I} + \mu(\boldsymbol{\nabla u} + (\boldsymbol{\nabla u})^{\mathrm{T}})$ is the fluid stress tensor, '+' and '−' denote two sides along the immersed boundary (as marked in figure 2), and $\boldsymbol{n}$ is the unit outward normal vector point from '−' side to '+' side. In the FSI of external flows, such as a flapping filament in a uniform flow (Tian *et al.* 2011*b*), the fluid stress exerted on the filament can be directly evaluated by (3.13). For internal flows, such as the case considered here, the elastic wall is only subjected to the internal fluid stress (i.e. σ^{-}). Williams *et al.* (2009) discussed two ways of accurately evaluating the fluid stress in a rigid channel flow and confirmed that it is reasonable to directly evaluate the fluid stress tensor at one grid point inward of the boundary. Here we extend this method to the FSI of a collapsible channel flow (moving boundary case), and find that interpolating the fluid stress tensor at 2.5 grid points inward of the moving boundary (at lattice E in figure 2) can accurately evaluate the fluid stress exerted on the elastic wall. The fluid stress at lattice E is evaluated by the inverse distance weighting of the fluid stress at the four nodes of lattice E: A, B, C and D.

The boundary conditions at the fluid–solid interface $\boldsymbol{X} = \boldsymbol{X}(s,t)$ are the no-slip, no-penetration and traction conditions,

$$\boldsymbol{u}(x,t) = \boldsymbol{U}(s,t), \quad \boldsymbol{f_t} = \sigma^{-} \cdot \boldsymbol{n}, \tag{3.14a,b}$$

where $\boldsymbol{f_t}$ is the hydrodynamic traction on the solid boundary. The resultant force exerted on the elastic wall by the fluid and the external pressure in (2.3) is evaluated by

$$\boldsymbol{F} = \sigma^{-} \cdot \boldsymbol{n} + P_e \boldsymbol{n}. \tag{3.15}$$

3.4. *Summary of the numerical method*

The fluid and structure solvers are coupled through a partitioned and weekly coupling approach, i.e. the flow and the structure solvers are solved sequentially only once at each time step. As a result, the boundary conditions at the fluid–solid interface mismatch by one half-step at the end of each time step. This coupling approach is computationally efficient, but it may cause numerical instability at low mass ratio due to the added mass effects (Borazjani, Ge & Sotiropoulos 2008; Tian *et al.* 2014). In this work, to enhance the numerical stability, an iterative feedback version of the IBM is applied at the fluid–solid interface, which allows for local flow reconstruction in the vicinity of the solid boundary. The iteration ensures that the displacement, velocity and traction boundary conditions at the fluid–solid interface are matched between the fluid and the solid boundary at each time step. The implementation of the weakly coupled FSI for the iterative IB-LBM algorithm is shown in the flowchart of figure 3 and is summarized as follows.

(1) Initialize the computation parameters.
(2) Stream the distribution function to obtain g_i.
(3) Compute the macroscopic variables: density ρ and the uncorrected velocity $\boldsymbol{u}$ using

$$\rho = \sum_i g_i, \quad \boldsymbol{u} = \frac{1}{\rho}\sum_i \boldsymbol{e}_i g_i. \tag{3.16a,b}$$

(4) Set iteration number (m) of IBM to 0.
(5) Interpolate the immersed boundary velocity $\boldsymbol{U}_{ib}^m$ using (3.10).
(6) Compute the Lagrangian force density $\boldsymbol{F}_{ib}^m(s,t)$ using (3.9).
(7) Spread $\boldsymbol{F}_{ib}^m(s,t)$ to the Eulerian fluid nodes around the immersed boundary to obtain $\boldsymbol{f}^m(\boldsymbol{x})$.
(8) Correct the Eulerian velocity near to the immersed boundary according to

$$\boldsymbol{u}^{m+1}(\boldsymbol{x}) = \boldsymbol{u}^m(\boldsymbol{x}) + \frac{\boldsymbol{f}^m(\boldsymbol{x})\,\mathrm{d}t}{2\rho(\boldsymbol{x})}. \tag{3.17}$$

(9) Increment iteration number m by 1.
(10) Repeat steps 5–9 until the velocity error at the immersed boundary is less than a pre-set criterion

$$Error = \frac{max\left(\sqrt{\left(\boldsymbol{U}_{ib}^m - \boldsymbol{U}(s,t)\right)^2}\right)}{U_0} \leq 5\times 10^{-3}. \tag{3.18}$$

(11) Interpolate the internal fluid stress and evaluate the total external force exerted on the elastic wall using (3.15).
(12) Solve the structure (2.3) and then update the coordinate $\boldsymbol{X}(s,t)$ and velocity $\boldsymbol{U}(s,t)$ of the elastic wall.
(13) Calculate g_i^{eq} using (3.4).
(14) Perform the collision step with the total Eulerian body force,

$$\boldsymbol{f}(x) = \sum_{m=1}^{m_{max}} \boldsymbol{f}^m(\boldsymbol{x}). \tag{3.19}$$

(15) Go to step 2 for next time-step.

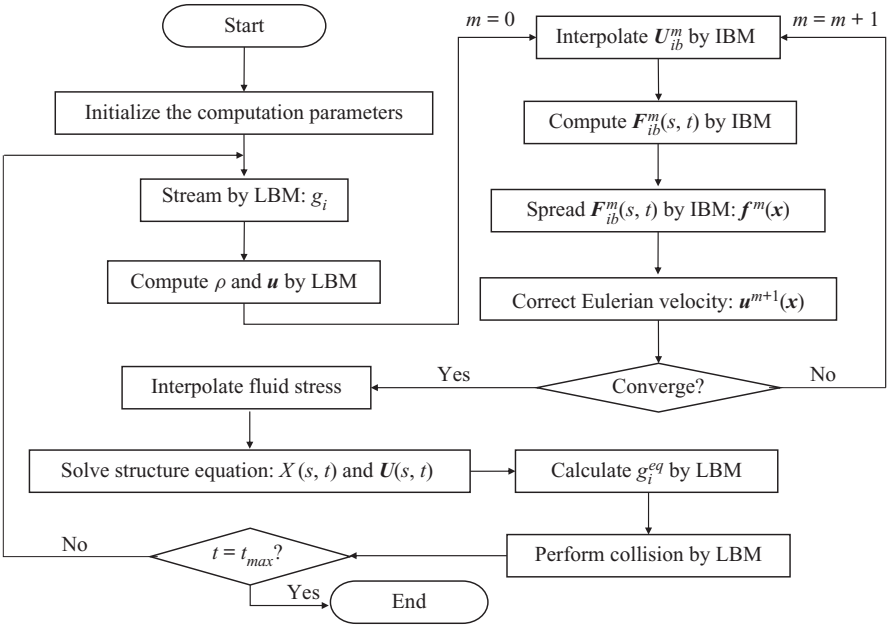

Figure 3. Flowchart of the iterative IB-LBM FSI algorithm.

To enhance the numerical stability, in step 12, 100 sub-steps are used in the structure solver at each time step (Tian *et al.* 2014; Tian 2014; Tian *et al.* 2015). The iterative IBM (from step 5 to step 9) may not show significant improvement for external flows. However, for confined FSIs such as the collapsible channel flow considered in this work, it does show significant improvement in results as the accuracy of the velocity near the immersed boundary has significant effect on the dynamics of the flexible wall (Huang & Tian 2019).

3.5. *Validation of the numerical method*

The IB-LBM FSI coupling strategy used here has been validated and successfully applied to many external flows in our previous publications (Tian *et al.* 2010, 2011*a*,*b*; Xu *et al.* 2018; Huang & Tian 2019; Ma *et al.* 2020). Further validations are conducted here focusing on the FSI in confined flows.

Steady flow in a one-sided collapsible channel is used to validate the current IB-LBM FSI solver for large-deformation FSI in a confined flow. An open multi-processing (OpenMP) parallel computing strategy has been incorporated into the code to accelerate the computation. Most computations are performed on an Intel Xeon CPU E5-2650 2.3 GHz workstation. Each time step of the unsteady simulation using the FSI solver requires 0.0014 CPU min (approximately 3.5 CPU min for $t/T = 1$, $T = D/U_0$ is the reference time). For the nonlinear dynamic analysis, approximately 4–7 days are required to advance the calculation to $t/T = 1000$.

3.5.1. *Steady collapsible channel flow*

To validate the IB-LBM FSI solver, we consider a one-sided collapsible channel flow (see figure 1*a*) and compare the results with those reported by Liu *et al.* (2009) who used an ALE FSI solver for this case. Three steady cases (labelled A, B and C) have been chosen with non-dimensional governing parameters given in table 1. Figure 4 shows the steady

Cases	Re	K_s	P_e
A	300	139	4.73
B	300	250	1.95
C	500	2400	1.95

Table 1. Non-dimensional parameters of the steady collapsible channel flow.

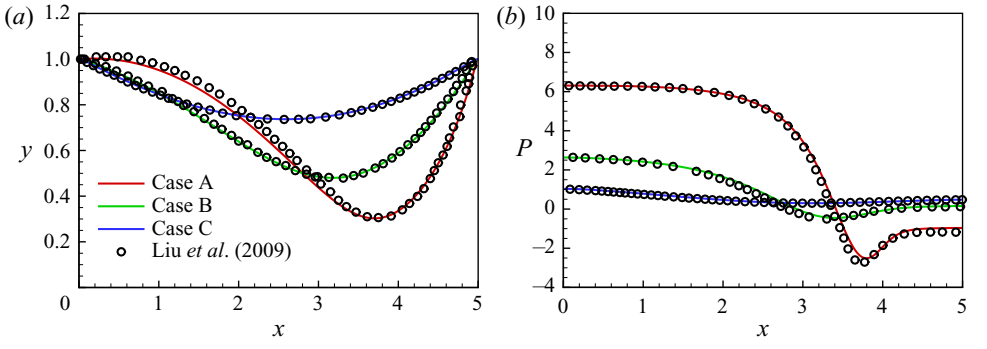

Figure 4. Comparison of steady solutions from current IB-LBM method and the fluid-beam model (FBM) of Liu *et al.* (2009). (*a*) Wall shape. (*b*) Pressure distribution.

shape of the elastic wall and the pressure distribution along the wall. It shows that the present results agree well with the numerical solutions of Liu *et al.* (2009).

3.5.2. *Flow-induced vibration of a highly flexible filament in a uniform flow*

In this section a flow-induced vibration of a highly flexible filament in a uniform flow has been simulated to validate the case in which the densities of the fluid and solid are very different. The filament has thickness h and length L with the leading edge fixed in a uniform incoming flow. The computational domain is a rectangular box ($x \in [-5L, 10L]$ and $y \in [-3L, 3L]$), and the grid size for the fluid and the filament are $0.02L$ and $0.01L$, respectively. The non-dimensional parameters for this case are

$$Re = \frac{\rho_{fluid} U_0 L}{\mu}, \quad M = \frac{\rho_{solid} h}{\rho_{fluid} L}, \quad K_s = \frac{Eh}{\rho U_0^2 L^2}, \quad K_b = \frac{EI}{\rho U_0^2 L^3}. \tag{3.20a–d}$$

Here $Re = 100$, $M = 1$, $K_s = 500$, $K_b = 0.0001$, $h/L = 1.29 \times 10^{-4}$ and $\rho_{solid}/\rho_{fluid} = 7751.94$. The simulated time history of the y-coordinate at the free end of the filament is shown in figure 5. Result shows good agreement with the numerical solutions of Wang *et al.* (2017).

3.5.3. *Mesh independence study*

In the mesh independence study four cases are chosen, and three lattice spacings are used: $\mathrm{d}x = 0.02$, $\mathrm{d}x = 0.01$ and $\mathrm{d}x = 0.005$. The solid mesh size is maintained at half of the lattice spacing. Simulation parameters for the four cases are given in table 2.

Figure 6 shows the y-coordinate time history of the mid-point of the upper elastic wall for the three mesh refinements. The solutions are converged. The difference between

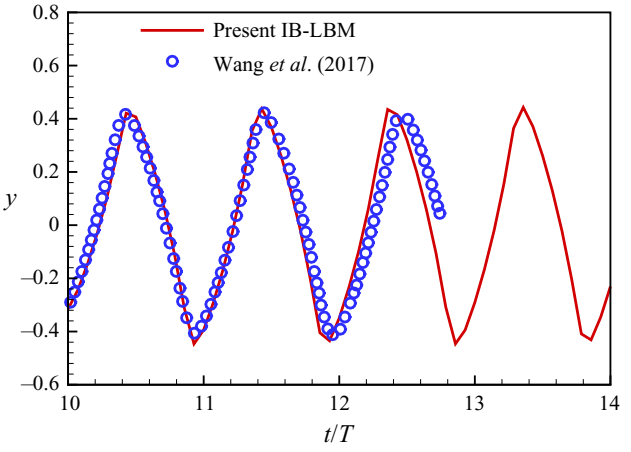

Figure 5. The y-coordinate time history of a flapping filament in a uniform flow.

Cases	Re	M	K_s	P_e
1	3000	10	2400	1.95
2	500	10	2400	1.95
3	500	20	2400	1.95
4	500	1	2400	10.0

Table 2. Simulation parameters of the grid independence study.

$\mathrm{d}x = 0.02$ and $\mathrm{d}x = 0.01$ is much larger than that between $\mathrm{d}x = 0.01$ and 0.005. Therefore, $\mathrm{d}x = 0.01$ with a total mesh size of 4000×140 is used in the rest of this work.

4. Results and discussion

Here the effects of governing parameters on the flow physics in a two-sided collapsible channel flow are studied. These parameters are the Reynolds number Re, structure-to-fluid mass ratio M and external pressure P_e. Extensive simulations are conducted by varying the parameters as follows: $100 \leq Re \leq 3000$, $0.3 \leq M \leq 100$, and $1 \leq P_e \leq 10$.

4.1. *Flow bifurcation: symmetry breaking*

Although the experimental study by Kounanis & Mathioulakis (1999) revealed that symmetry breaking of the flow downstream of the throat might be a potential mechanism for the onset of self-excited oscillations, the role of symmetry breaking in the instability of this collapsible system needs to be further explored. In this section, therefore, we will identify the critical Reynolds number for symmetry breaking of the flow and explore the role of symmetry breaking in the instability of the collapsible system. The Reynolds number is increased from 220 to 540 with an increment of 20, and other non-dimensional governing parameters are $M = 1$, $K_s = 2400$ and $P_e = 1.95$. In order to demonstrate where the qualitative change of the flow field occurs, the streamlines of eight typical cases are shown in figure 7. It is found that, from $Re = 220$ to $Re = 300$, the flow is stable and symmetric with a single jet downstream of the collapsible walls, and the size

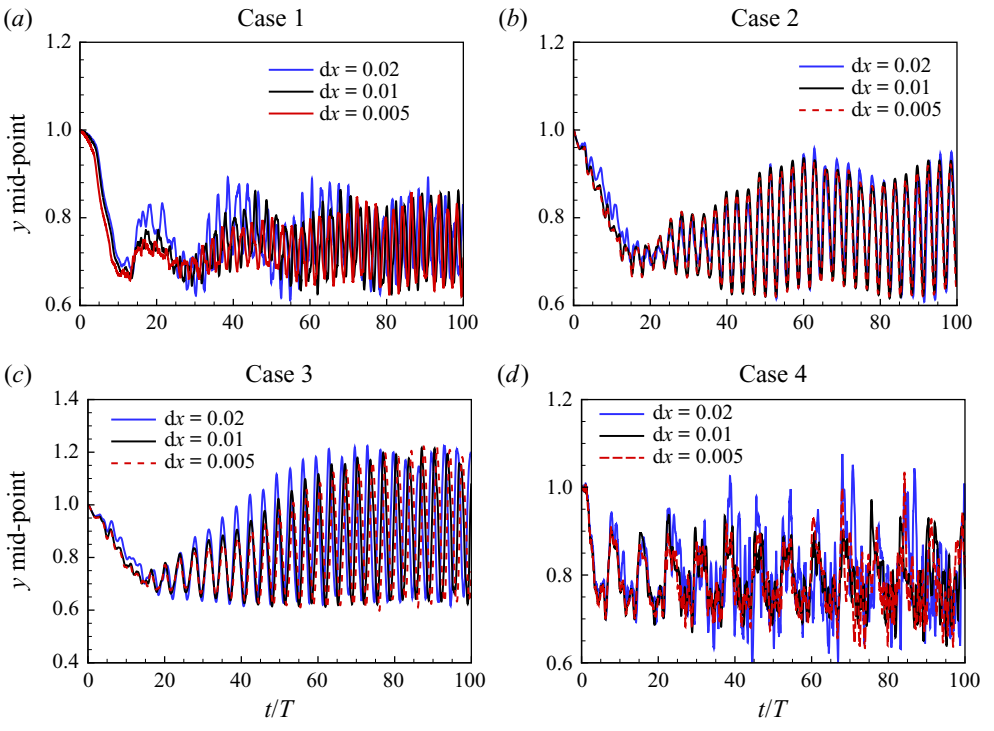

Figure 6. Mesh independence study: the y-coordinate time history of the mid-point ($x = 2.5$ initially) of the upper elastic wall. (*a*) Case 1. (*b*) Case 2. (*c*) Case 3. (*d*) Case 4.

of recirculation regions is equal on both sides of the jet flow, which is consistent with the experimental observation by Ohba, Skurai & Oka (1997). Even if 2-D channels and 3-D tubes are different in the geometry, 2-D simulations and 3-D collapsible tubes in experiments share some similarities in the basic physical explanation of the instabilities (Luo *et al.* 2008). Luo & Pedley (1996) confirmed that some features of the oscillation found in a numerical 2-D collapsible channel are qualitatively similar to the experimental observation in a 3-D collapsible tube.

The symmetry breaking occurs at $Re = 320$ with a corner recirculation region on the upper wall much larger than that on the lower wall. The flow reaches a new stable asymmetric state, and the jet is attached to either side of the channel depending on the initial perturbation in the simulation. Previous studies of a 2-D indented rigid channel attributed the occurrence of a symmetry breaking bifurcation to a supercritical pitchfork bifurcation in solving the Navier–Stokes equations (Sobey & Drazin 1986). Above a certain critical Reynolds number for a specific geometry, two stable solutions co-exist which are confirmed by Battaglia *et al.* (1997) in the numerical study of 2-D sudden expansion channel flow. At $Re = 440$, the asymmetry is strengthened, and a third recirculation region appears on the lower wall. Such asymmetry is sustained, and the size of the recirculation regions increases with Re. At $Re = 520$, there is still a stable jet flow attaching to the lower wall. Finally, the flow becomes unstable at $Re = 540$.

In order to discuss the critical Reynolds number, the lengths of recirculation zones are shown in figure 8. Figure 8(*a*) defines how the lengths of these zones are measured, and figure 8(*b*) is the bifurcation diagram which shows the effect of Re on the length of the recirculation zones formed downstream of the throat. Similar bifurcation analysis

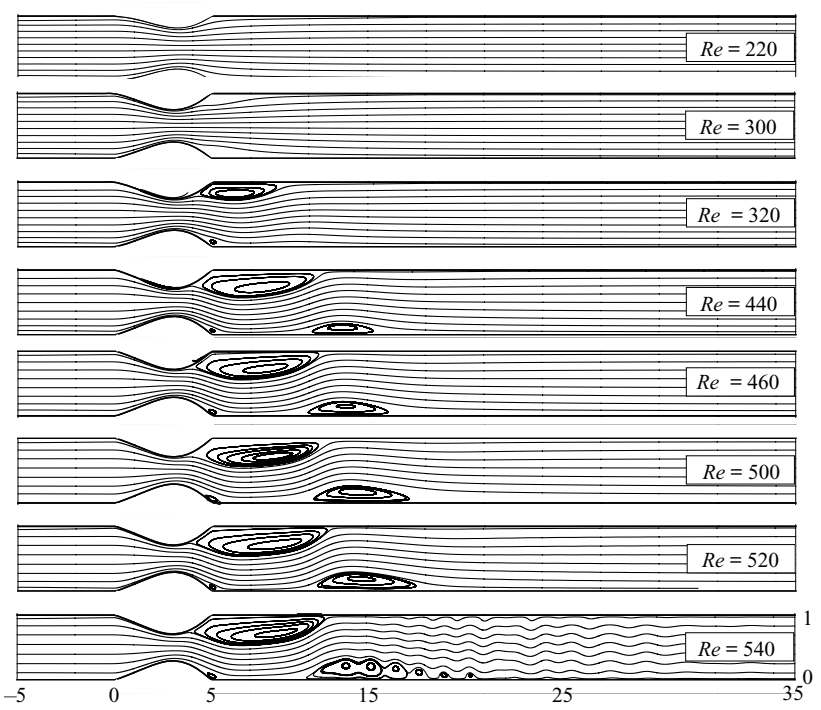

Figure 7. Streamlines for different Reynolds numbers Re with $M = 1$, $K_s = 2400$ and $P_e = 1.95$.

can be found in the study of flow through a symmetric rigid channel featuring a sudden contraction-expansion (Rocha, Poole & Oliveira 2007; Oliveira *et al.* 2008). It is clear that the system experiences the supercritical pitchfork bifurcation as the Reynolds number increases. At $Re = 320$, a new static equilibrium is established, and for $Re > 400$, a third recirculation region appears on either channel wall. The symmetry breaking of the jet flow in the parameter space investigated here (i.e. $Re = 220$–540 with $M = 1$, $K_s = 2400$ and $P_e = 1.95$) does not induce any oscillation of the elastic channel walls.

4.2. *Dynamic behaviours in M-Re plane and routes to chaos*

Here the dynamic behaviours in M–Re plane and possible routes to chaos are discussed. Simulations are conducted by varying the Reynolds number from 100 to 3000 with an increment of 50 and the mass ratio M from 0.3 to 100. Other dimensionless parameters are $K_s = 2400$ and $P_e = 1.95$.

Figure 9 shows the motion states of the collapsible system over $M \in (0.3, 100)$ and $Re \in (100, 1000)$, where the motion states are divided into steady, periodic, period-doubling, quasi-periodic and chaotic states which are determined by using the time history of wall motion trajectory, power spectral density (PSD), phase portrait and estimated dominant Lyapunov exponent. Here non-dimensional time of $t/T = 400 - 1000$ is used for the nonlinear dynamics analysis, to exclude the influence from the initial transient behaviour. At $M = 0.3$, only four cases are run as the simulations suffer from numerical instabilities for $Re > 400$. Figure 9 demonstrates that the dynamic behaviours of the system are very complex. Specifically, the chaotic motion occurs mainly at high Re and low mass ratios M or low Re and high mass ratios M. The continuity of the chaotic distribution

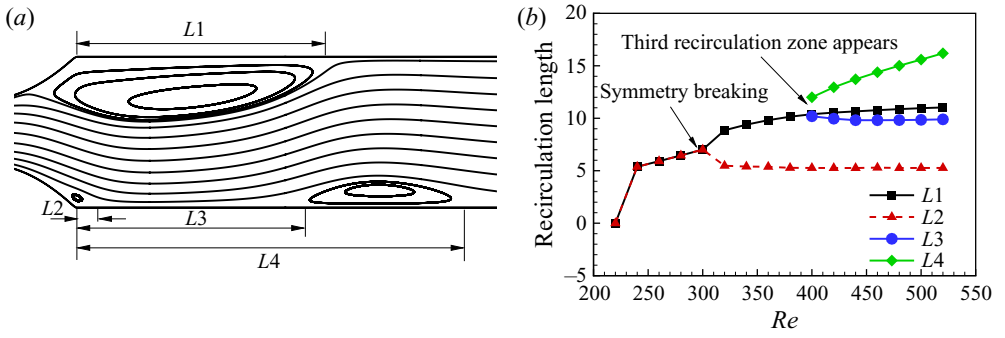

Figure 8. Quantitative results of the symmetry-broken solutions as the Reynolds number is increased: (*a*) schematic diagram of how the lengths of recirculation zones are measured; *L*1 and *L*2 are defined as the horizontal distance from the start point of the downstream rigid part of the channel to the right edge point of the pair of recirculation zones that appear first, and *L*3 and *L*4 are the horizontal distance from the start point of the downstream rigid part of the channel to the left and right edge of the third recirculation zone, respectively. (*b*) Bifurcation diagram.

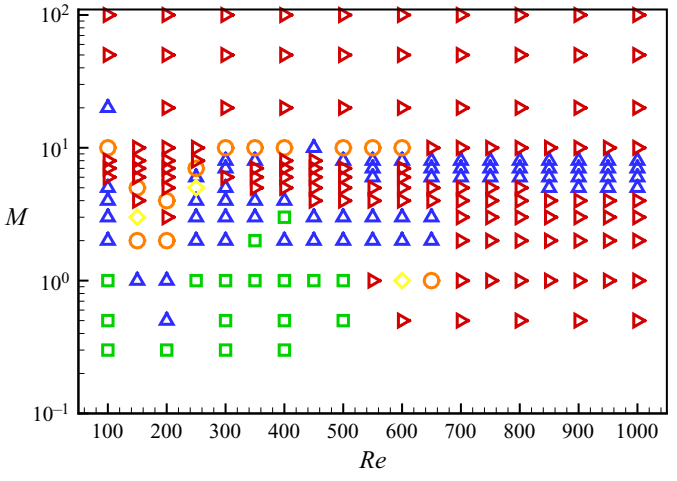

Figure 9. Motion state diagram in the $Re - M$ parameter space with $K_s = 2400$, $P_e = 1.95$: □, green - steady; △, blue - periodic; ♢, yellow – period-doubling; ◯, orange – quasi-periodic; ▷, red – chaotic.

is interrupted at $Re = 250$, $M = 6$ and $M = 7$, which will be discussed in § 4.2.2. The steady motion occurs at low mass ratios ($M \leq 3$). Taking the case of fixed mass ratio $M = 1$ with varying Re as an example, the system is steady at $Re = 100$. An increase of the Reynolds number results in the loss of static equilibrium via supercritical Hopf bifurcation, leading to a periodic limit cycle oscillation at $Re = 150$ and $Re = 200$. For $250 \leq Re \leq 500$, the system is steady. The system becomes chaotic at $Re = 550$. However, a period-doubling state is observed at $Re = 600$. The system reaches chaotic motion again via a quasi-periodicity route if the Reynolds number is further increased, similar to the Ruelle–Takens–Newhouse scenario (Ruelle & Takens 1971; Newhouse *et al.* 1978).

At $M = 3$, the system is in a periodic state at $Re = 100$ and then reaches a chaotic state at $Re = 200$ via the period-doubling route. This process is similar to the classical Feigenbaum scenario (Feigenbaum 1978, 1979) of the route to chaos. For $6 \leq M \leq 10$, most of the motion states switch back and forth between periodic and chaotic as

Re is increased. A similar phenomenon can also be observed for $650 \leq Re \leq 1000$ as M is increased. For high mass ratio at $M = 50$ and 100, only chaotic states are observed.

In order to discuss the flow physics associated with the states shown in figure 9, the transition process from steady to chaotic motion by fixing $M = 1$ and varying Re is discussed in § 4.2.1 and that by fixing $Re = 250$ and varying M is presented in § 4.2.2.

4.2.1. *Effects of Re*

Here we first discuss $M = 1$, $Re = 100$, 200, 500, 550, 600, 650, 800, 1000, 2000 and 3000, and then discuss $M = 10$, $Re = 1000$, 2000 and 3000.

Figure 10 shows the y-coordinate time history, the PSD and phase portrait consisting of the y-velocity vs y-coordinate of the mid-point of the upper collapsible channel wall for $M = 1$ and different values of Re. Figure 11 displays the corresponding vorticity contours to discuss the physical mechanisms associated with these motion states.

At $Re = 100$ and $Re = 500$, as shown in figures 10(a) and 10(g), the channel wall remains at its equilibrium position. A fixed point in the phase portrait (see figures 10c and 10i) indicates that the system is in a steady state at these Re. This is also revealed by a very low energy level of the PSD in figures 10(b) and 10(h). At $Re = 200$, the time series in figure 10(d) displays periodic oscillations. In figures 10(e) and 10(f) the appearance of a fundamental frequency f_1 and its harmonics (i.e. $2f_1$, $3f_1$ etc) and a single limit cycle in the phase portrait indicate that the system undergoes a period-1 limit cycle oscillation.

At $Re = 550$, the system experiences a chaotic motion, which is reflected by the broadband PSD in figure 10(k) and the chaotic attractor of the phase portrait in figure 10(l). Similar nonlinear dynamic characteristics can also be found at $Re = 800$ in figures 10(t) and 10(u). Figures 10(j) and 10(s) show that the chaotic oscillations involve small non-repetitive noise-like fluctuations. To further examine the chaotic motion, the dominant Lyapunov exponents λ are estimated by using the time-delay method of Wolf *et al.* (1985). An open source MATLAB code (Wolf 2021) is used to calculate λ based on a time series of y velocity-displacement data. See Wolf *et al.* (1985) for more details. This method has been adopted by Connell & Yue (2007) and Goza *et al.* (2018) to identify the chaotic motion of flapping flags. Note that a zero or near-zero value of λ corresponds to a non-chaotic motion state, while a positive value of λ indicates a chaotic motion state, and a negative value of λ represents a steady state. As the time-delay method of Wolf *et al.* (1985) only allows the estimation of non-negative Lyapunov exponents, the dominant Lyapunov exponents for steady state are not estimated here. The time series of the y velocity-displacement data is used in the phase space reconstruction. The computed results of λ for $M = 1$ at typical Re values are shown in table 3. The estimated dominant Lyapunov exponents at $Re = 550$ and $Re = 800$ are $\lambda = 0.0385$ and $\lambda = 0.0417$, respectively. These relatively large positive values of λ ($\sim$ of order 10^{-2}) support that the motion type at $Re = 550$ and $Re = 800$ is chaotic.

At $Re = 600$, the appearance of a subharmonic frequency $0.5f_1$ in the PSD (see figure 10n) and multiple limit cycles in the phase space (see figure 10o) indicate that the system experiences a period-doubling bifurcation. Figure 10(m) shows the regular oscillations for the period-doubling motion state. When the Reynolds number is further increased to $Re = 650$, a quasi-periodic motion state is identified, which is confirmed by the appearance of second- and third-fundamental frequencies (i.e. incommensurate frequencies f_2 and f_3, f_2/f_1 and f_3/f_1 are irrational) in the PSD of figure 10(q) and the limit torus in the phase space of figure 10(r).

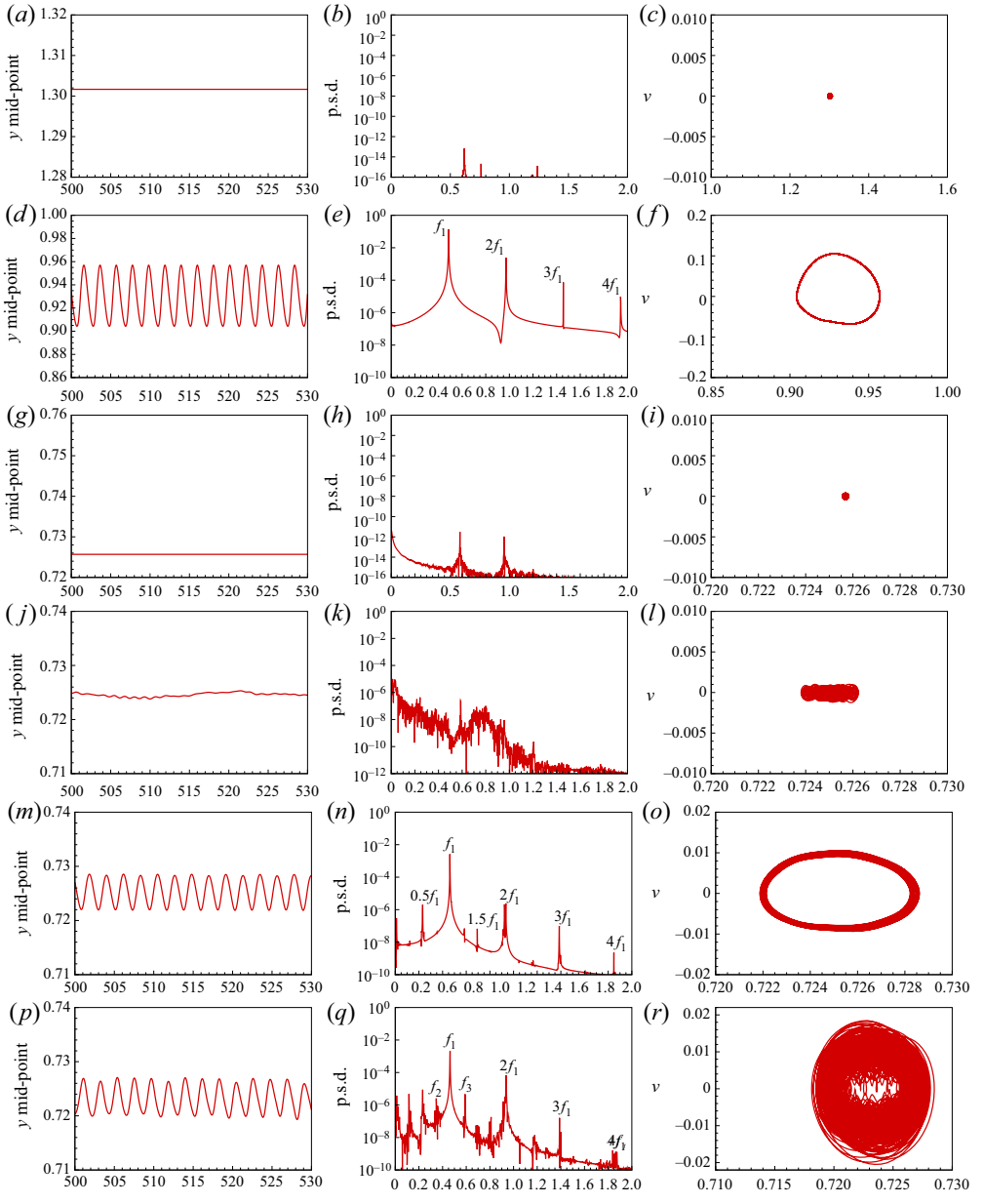

Figure 10. (*a–r*). For caption see on next page.

With the introduction of two new incommensurate frequencies, the multiple limit cycles at $Re = 600$ turn into a dense toroidal structure (see figure 10*r*). Figure 10(*p*) shows the quasi-periodic oscillations of the mid-point of the upper elastic channel wall at $Re = 650$.

From figure 11, it is found that the elastic channel walls bulge outward at $Re = 100$. At $Re = 200$, the walls undergo a mode-2 shaped deformation (i.e. with two half-wavelengths along the elastic wall). The walls indent inward of the channel with a further increase of Re. Whether the collapsible walls bulge outward or indent inward is determined by the resultant force acting on the elastic walls, which consists of the external pressure P_e and

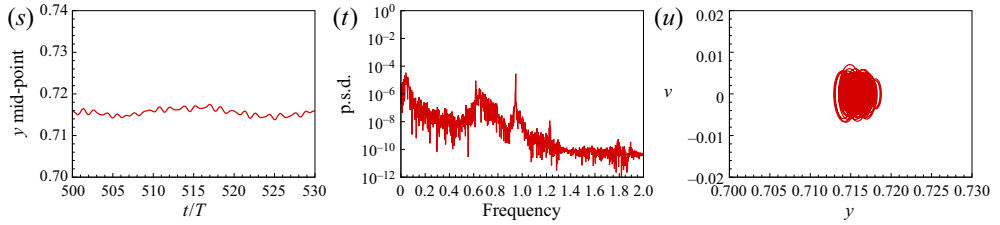

Figure 10 (cntd). The time history of the y-coordinate of the mid-point ($x = 2.5$ initially) at the upper elastic channel wall at various Reynolds numbers Re with $M = 1$, $K_s = 2400$, $P_e = 1.95$. Power spectral density and phase portrait in displacement-velocity (y–v) space. The frequency in the PSD is normalized by U_0/D. Here $Re = 100$: steady state; $Re = 200$: periodic state; $Re = 500$: steady state; $Re = 550$: chaotic state; $Re = 600$: period-doubling state; $Re = 800$: chaotic state. Plot parameters: (*a*) $Re = 100$: steady state; (*b*) $Re = 100$: low energy; (*c*) $Re = 100$: fixed point; (*d*) $Re = 200$: periodic state; (*e*) $Re = 200$: fundamental frequency f_1 and its harmonic frequencies, $2f_1$, $3f_1$; (*f*) $Re = 200$: single limit cycle; (*g*) $Re = 500$: steady state; (*h*) $Re = 500$: low energy; (*i*) $Re = 500$: fixed point; (*j*) $Re = 550$: chaotic state; (*k*) $Re = 550$: broadband continuous spectrum; (*l*) $Re = 550$: chaotic attractor; (*m*) $Re = 600$: period-doubling state; (*n*) $Re = 600$: the arise of subharmonic frequencies $0.5f_1$, $1.5f_1$; (*o*) $Re = 600$: multiple limit cycles; (*p*) $Re = 650$: quasi-periodic state; (*q*) $Re = 650$: the arise of second- and third fundamental frequencies, f_2, f_3; (*r*) $Re = 650$: limit torus; (*s*) $Re = 800$: chaotic state; (*t*) $Re = 800$: broadband continuous spectrum; (*u*) $Re = 800$: chaotic attractor.

M	*Re*	Lyapunov exponent (λ)	Motion state
1	100	NA	steady
1	200	0.0021	periodic
1	500	NA	steady
1	550	0.0385	chaotic
1	600	0.0076	period-doubling
1	650	0.0124	quasi-periodic
1	800	0.0417	chaotic

Table 3. Estimated dominant Lyapunov exponents and corresponding motion states of the system: $K_s = 2400$, $P_e = 1.95$. Here NA means not applicable as only the estimation of non-negative Lyapunov exponents are allowed for the time-delay method of Wolf *et al.* (1985).

the fluid stress. The normal component of the external force is the transmural pressure $p - P_e$ (i.e. internal minus external pressure), which is affected by the pressure loss in the channel. As seen from figure 12, the pressure inside the channel is large at $Re = 100$ due to higher pressure loss, so that a positive transmural pressure (i.e. $p - P_e > 0$) is developed and pushes the elastic walls outward. For $Re > 200$, the pressure inside the channel is small enough as the pressure loss becomes smaller, so that a negative transmural pressure ($p - P_e < 0$) causes the elastic walls to move inward. This phenomenon is consistent with the finding of Luo *et al.* (2008) that the wall curvature is determined by the transmural pressure.

In addition, the physical mechanisms that lead to the different motion states are varied. For $Re = 100$, the viscosity is strong enough to damp out any small disturbance. The very positive transmural pressure (i.e. $p - P_e \sim 2$) along the whole elastic channel walls and the relatively small wall inertia (i.e. $M = 1$) lead to a steady state at $Re = 100$. The transmural pressure decreases as the Reynolds number increases. At $Re = 200$, the configuration of the elastic walls contains two half-wavelengths. The system is unstable to this mode 2 perturbation due to a mode 2 transmural pressure distribution formed where a positive transmural pressure at the anterior segment of the collapsible walls (i.e. $x \leq 1$) pushes the

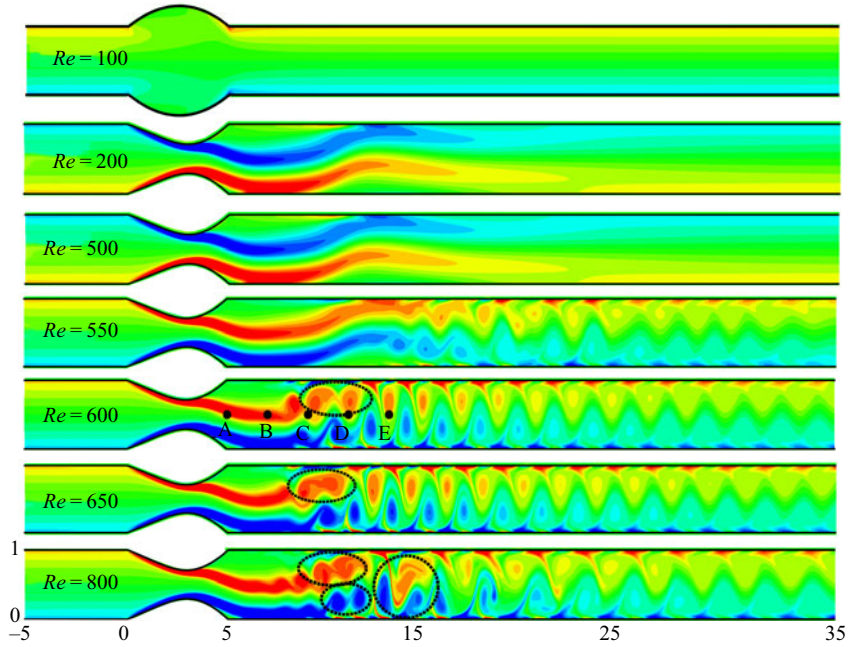

Figure 11. Instantaneous vorticity contours at $t/T = 100$ for various Re with $M = 1$, $K_s = 2400$ and $P_e = 1.95$. The vorticity ranges from -10 (blue) to 10 (red). Note: the aspect ratio (length/width) is set to 0.3 for an overview of the whole flow field. Here A(5, 0.5), B(7, 0.5), C(9, 0.5), D(11, 0.5) and E(13, 0.5) are five probe points. Animations of the vorticity contours for $Re = 200$, $Re = 550$, $Re = 600$, $Re = 650$ and $Re = 800$ are provided in supplementary movies 1 to 5 available at https://doi.org/10.1017/jfm.2021.710.

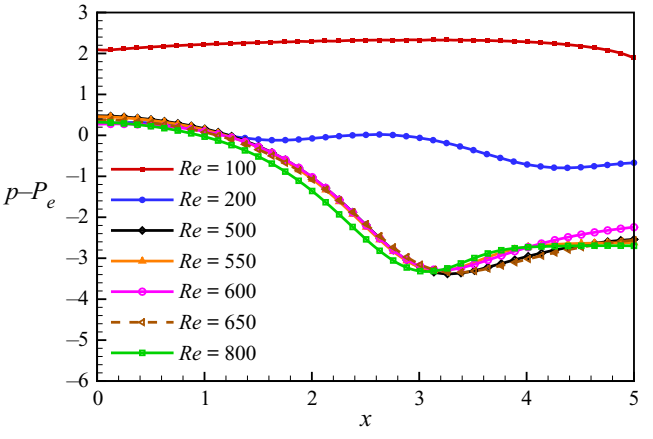

Figure 12. The transmural pressure distributions along the upper elastic channel walls for different Re with $M = 1$, $K_s = 2400$ and $P_e = 1.95$.

walls outward and a negative transmural pressure at the remaining part of the collapsible walls (i.e. $1 < x \leq 5$) causes the walls to move inward. As a result, this unbalanced transmural pressure along the collapsible walls causes the self-excited oscillations of the walls. The self-excited oscillations at $Re = 200$ can be explained as follows which has been recognized as one of the main mechanisms for the oscillations of collapsible tubes (Luo *et al.* 2008). The flow accelerates to higher speed at the downstream end of the elastic walls

as the channel becomes more constricted. Then the pressure decreases due to conservation of mass, which enhances the constriction further. This in turn causes the increase of viscous resistance in the vicinity of the constriction, either through viscous dissipation in the boundary layers, or through flow separation. As a result, upstream pressure will rise due to a higher pressure drop required to maintain the flow rate, causing the upstream half of the elastic walls to bulge out further, and then forcing the reopening of the constriction. At $Re = 500$, a very negative transmural pressure is observed in figure 12, which causes the channel walls to collapse and indent inward. Furthermore, as shown in figure 11, at $Re = 500$, flow separation occurs slightly downstream of the narrowest point, and a stable but asymmetric jet is developed with the jet attaching to the lower wall. Owing to the Coanda effect, such asymmetry can be maintained, resulting in an increase in the velocity and a decrease in the pressure near the lower wall. The very negative transmural pressure, a stable jet flow without vortex shedding and the weak effect of the wall inertia lead to a steady configuration at $Re = 500$. The flow becomes unsteady if the Reynolds number further increases. As seen in figure 11, at $Re = 550$, the jet flow between the recirculation zones loses its stability and breaks into small vortices that are transported downstream. Then the flow becomes time dependent, and the channel walls enter a chaotic motion state.

At $Re = 600$, figure 11 shows that there is vortex shedding downstream of the throat. To trace the PSD of the streamwise velocity, five probe points (i.e. A(5, 0.5), B(7, 0.5), C(9, 0.5), D(11, 0.5) and E(13, 0.5) as shown in figure 11 at $Re = 600$) are monitored. Figure 13 shows that the streamwise velocities at five probe points are all in period-doubling oscillations as indicated by the subharmonic frequencies $0.5f_1$ and $1.5f_1$ in the PSD. The periodic component is attributed to the periodic shedding of vortices downstream of the throat that feeds back periodic perturbations on the elastic walls. The partial pairing of two adjacent vortices (as marked in figure 11) downstream of the elastic walls further feeds back subharmonic perturbations on the elastic walls that trigger period-doubling oscillations of the elastic walls. This process is further demonstrated by supplementary movie 3. A similar vortex pairing process can be found in the coherent structure interactions in a mixing layer (Hussain 1986) and in the vortex shedding in an arterial stenosis (Bluestein *et al.* 1999). Results in figure 13 show that the PSD of the subharmonic frequency $0.5f_1$ increases in the streamwise direction and reaches its peak value at D(11, 0.5) indicating that a partial pairing process occurs between C(9, 0.5) and D(11, 0.5), which further supports the conclusion that the period-doubling oscillations at $Re = 600$ are caused by the periodic vortex shedding and the partial pairing of two adjacent vortices.

As the Reynolds number is further increased to $Re = 650$, periodic vortex shedding downstream of the throat is also observed. Apart from that, there is a merging of adjacent three vortices at $x \approx 10$ (as marked in figure 11) that feeds back additional perturbations on the elastic walls leading to quasi-periodic oscillations in the channel walls. The merging process is further demonstrated by supplementary movie 4.

At $Re = 800$, the vortex merging at $x \approx 10$ and the interactions between the vortices on the upper and lower walls downstream at $x \approx 14$ cause the walls to settle into chaotic oscillations featuring small noise-like fluctuations as shown in supplementary movie 5. Further simulations have been conducted for a single-sided collapsible channel. There is no vortex shedding downstream of the throat due to mild stenoses (e.g. 28 % diameter reduction at $Re = 1000$) formed with only one collapsed wall. Therefore, the system is steady for $Re > 300$, and the period-doubling, quasi-periodic and chaotic motion states caused by the interactions between the collapsed wall and the vortices are not observed.

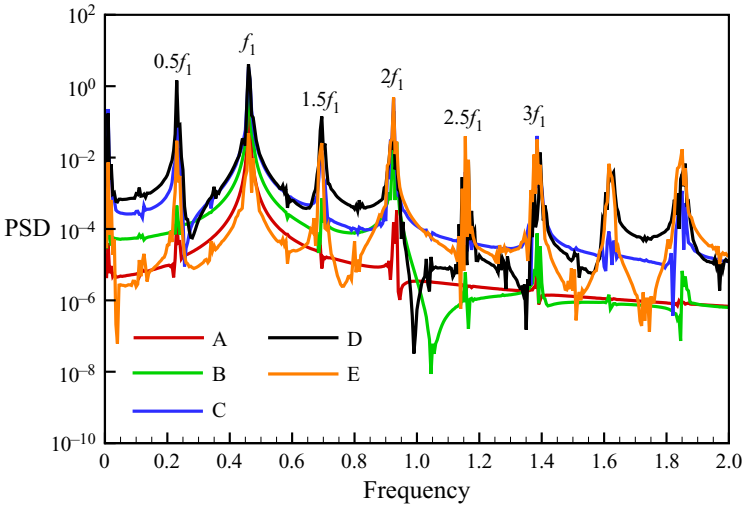

Figure 13. The PSD of the streamwise velocity u at five probe points: A(5, 0.5), B(7, 0.5), C(9, 0.5), D(11, 0.5) and E(13, 0.5) for $Re = 600$.

The motion of flexible walls is chaotic at high Reynolds number for mass ratios of 1 and 10 between which there are periodic and period-doubling states. In order to compare the chaotic behaviours at high Reynolds numbers at different mass ratios, two mass ratios ($M = 1$ and 10) are considered at $K_s = 2400$, $P_e = 1.95$ and $Re = 1000$, 2000 and 3000. Figure 14 shows the time history of the y-coordinate of the mid-point ($x = 2.5$ initially) of the upper and lower elastic walls. For $M = 1$ and $Re = 1000$, as seen in figure 14(a), there is no obvious oscillation of the elastic walls after collapse. When the mass ratio increases to $M = 10$, the elastic walls gradually start to develop self-excited oscillations after collapse (see figure 14b). When the Reynolds number increases to $Re = 2000$ for $M = 1$, the elastic walls experience irregular small-amplitude oscillations (approximately $0.02D$ as shown in figure 14c), and such oscillations are more evident and irregular at $Re = 3000$ (see figure 14e). Figures 14(d) and 14(f) show that, for $M = 10$ at $Re = 2000$ and $Re = 3000$, the elastic walls undergo much larger-amplitude oscillations (approximately $0.1D$) because of the higher inertia.

Instantaneous vorticity contours for various Re at $M = 1$ and $M = 10$ are presented in figure 15. Overall, the diffusion of vortices decreases with the increase of Reynolds number due to the reduced viscosity. As a result, stronger vortices and thinner boundary layers are observed as the Reynolds number increases. As seen from figure 15(a) for $M = 1$, a streaming jet flow attaches to the lower wall at $Re = 1000$. The jet flow between the recirculation zones loses its stability and breaks up into small vortices that are transported downstream. At $Re = 2000$, the region of shed vortices is closer to the upstream end of the elastic walls when compared with $Re = 1000$. Moreover, for $x \geq 10$ at $Re = 2000$, a clear reverse Kármán vortex street (indication of a jet flow) is observed with two staggered rows of vortices being transported downstream. The vortices are counterclockwise (positive vorticity) in the upper row and clockwise (negative vorticity) in the lower row. It is interesting to note that the instantaneous vorticity contours at $Re = 3000$ show two non-staggered rows of vortex street right at the end of the elastic walls, but they lose stability and interact with each other from $x = 8$. In addition, the system loses stability at $Re = 2000$ and $Re = 3000$, and the elastic walls move up and down alternately, generating vorticity waves downstream. Such instability at $Re = 2000$ and $Re = 3000$ can also be explained by the shear layer instabilities as demonstrated in

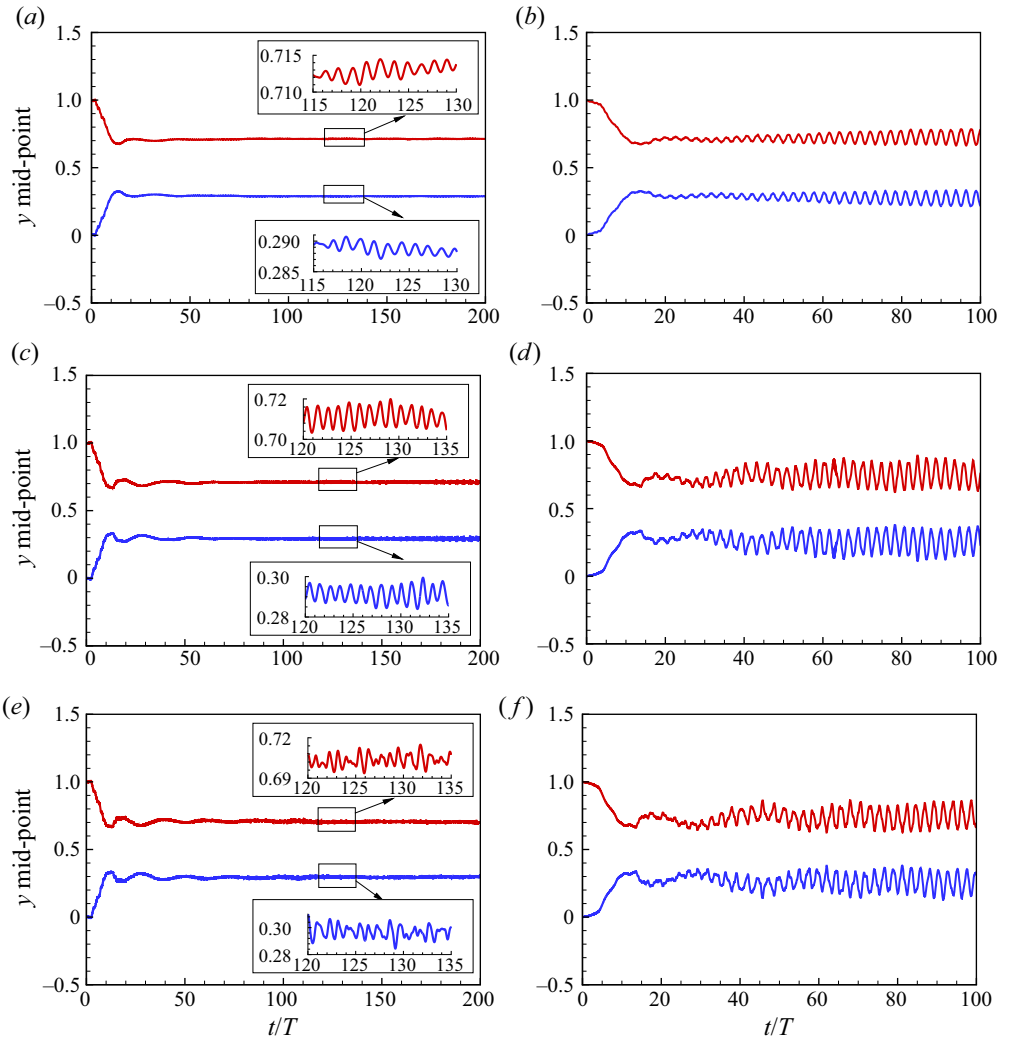

Figure 14. The y-coordinate time history of the mid-point ($x = 2.5$ initially) at the collapsible channel walls at various Reynolds numbers Re with $M = 1$ and $M = 10$. Other dimensionless parameters are $K_s = 2400$, $P_e = 1.95$. The red line and blue line represent the y-coordinate of the upper and lower elastic wall, respectively. Plot parameters: (*a*) $M = 1$, $Re = 1000$; (*b*) $M = 10$, $Re = 1000$; (*c*) $M = 1$, $Re = 2000$; (*d*) $M = 10$, $Re = 2000$; (*e*) $M = 1$, $Re = 3000$; (*f*) $M = 10$, $Re = 3000$.

§ 4.2.1. As can be seen from figure 15(*a*), at $M = 1$ and $Re = 1000$, the shed vortices are far downstream from the elastic walls and, thus, have a weak impact on their motion. However, at $Re \geq 2000$, the shed vortices, which are close to the mid-point of the elastic walls, feeds back perturbations on the elastic walls to produce small-amplitude self-excited oscillations in the elastic walls.

From the above analysis, it is found that the vortex shedding caused by shear layer instabilities at $Re = 2000$ and $Re = 3000$ are responsible for the onset of self-excited oscillations. As seen from figure 15(*b*) for $M = 10$, at $Re = 1000$, a series of vortex pairs dissipating quickly downstream are observed, while an asymmetric jet flow is observed at $M = 1$. The higher amplitude of the self-excited oscillations at $M = 10$ than at $M = 1$

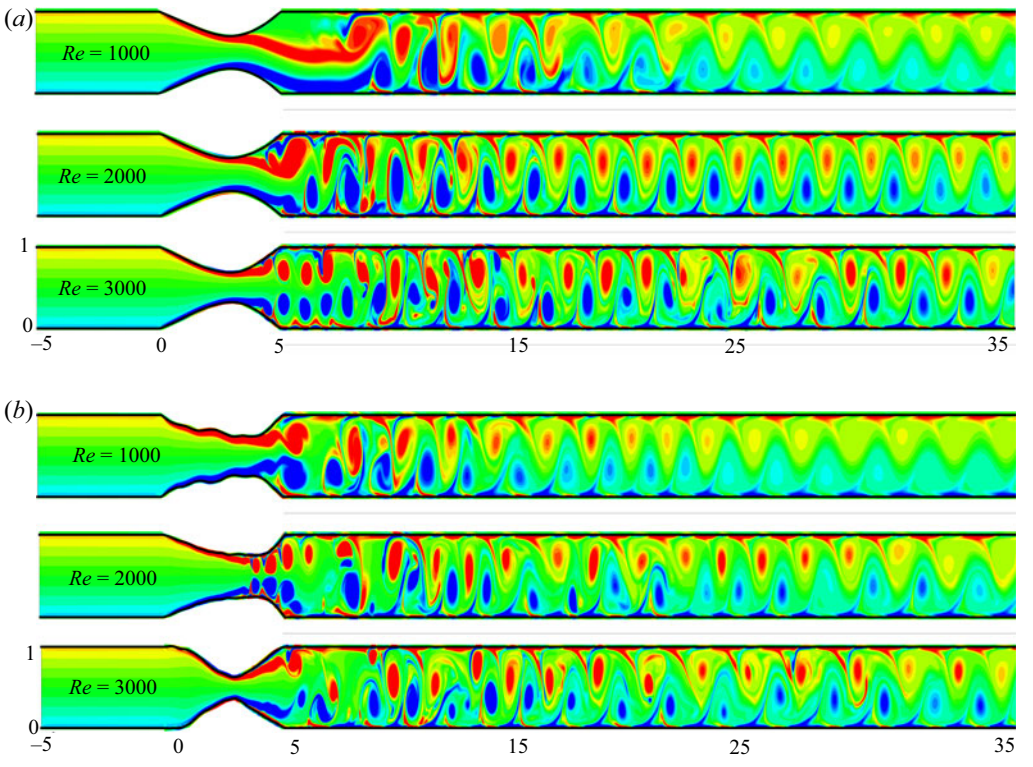

Figure 15. Instantaneous vorticity contours under different Re at $t/T = 200$ with $M = 1$ and $M = 10$, $K_s = 2400$ and $P_e = 1.95$. The vorticity ranges from -10 (blue) to 10 (red). Note: the aspect ratio (length/width) is set to 0.3 for an overview of the whole flow field. Plot parameters: (*a*) $M = 1$ with $Re = 1000$, 2000 and $Re = 3000$; (*b*) $M = 10$ with $Re = 1000$, 2000 and 3000.

indicates stronger FSIs between the jet and the elastic walls at the higher mass ratio. In this situation, the whole of the elastic walls undergo large-amplitude oscillations (see figure 15(*b*) at $Re = 1000$ and $M = 10$). The oscillations become regular at $Re = 1000$ when the mass ratio increases from $M = 1$ to $M = 10$ (see figure 14).

For $M = 10$, the large-amplitude and irregular oscillations at $Re = 2000$ and $Re = 3000$ are the results of interactions between different instability modes (i.e. the instabilities induced by the shedding of vortices at high Re and the travelling-wave flutter induced by the wall elasticity at high M).

4.2.2. *Effects of M*

At $Re = 250$, there are no vorticity waves convecting downstream of the elastic walls when M varies from 1 to 8. Therefore, the wall inertia plays an important role in inducing the different motion states of the elastic walls. Six cases ($M = 1$, 4, 5, 6, 7 and 8) are analysed in detail. Figure 16 shows the corresponding y-coordinate time history, the PSD and phase portrait of y-velocity vs y-coordinate of the mid-point at the upper collapsible wall. The travelling-wave flutter of $M = 5$ is shown in figure 17. Figure 18 displays the corresponding instantaneous vorticity contours of the flow field.

Similar to $Re = 200$ and $M = 1$ in figure 10, a steady motion is observed at $Re = 250$ and $M = 1$, as demonstrated by the wall remaining at its equilibrium position in figure 16(*a*), the low energy level in figure 16(*b*) and the fixed point in the phase portrait

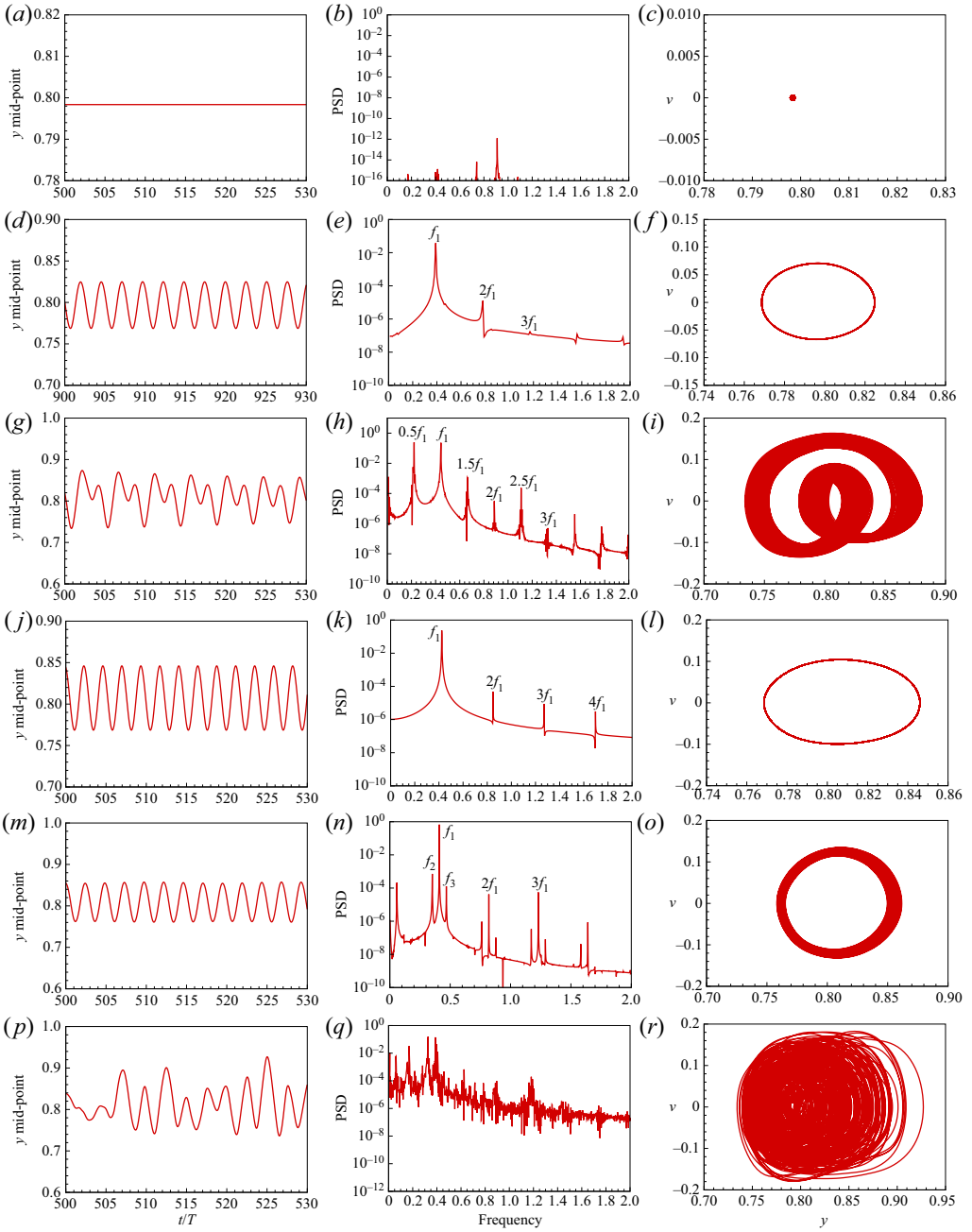

Figure 16. The time history of the y-coordinate of the mid-point ($x = 2.5$ initially) of the upper elastic wall under different mass ratios M with $Re = 250$, $K_s = 2400$, $P_e = 1.95$. Power spectrum density (PSD) and phase portrait in displacement-velocity (y-v) space. The frequency in the PSD is normalized by U_0/D. Here $M = 1$: steady state; $M = 4$: periodic state; $M = 5$: period-doubling state; $M = 6$: periodic state; $M = 7$: quasi-periodic state; $M = 8$: chaotic state. Plot parameters: (*a*) $M = 1$: steady state; (*b*) $M = 1$: low energy; (*c*) $M = 1$: fixed point; (*d*) $M = 4$: periodic state; (*e*) $M = 4$: fundamental frequency f_1 and its harmonic frequencies $2f_1$, $3f_1$; (*f*) $M = 4$: limit cycle; (*g*) $M = 5$: period-doubling state; (*h*) $M = 5$: the arise of subharmonic frequencies $0.5f_1$, $1.5f_1$; (*i*) $M = 5$: multiple limit cycles; (*j*) $M = 6$: periodic state; (*k*) $M = 6$: fundamental frequency f_1 and its harmonic frequencies $2f_1$, $3f_1$; (*l*) $M = 6$: limit cycle; (*m*) $M = 7$: quasi-periodic state; (*n*) $M = 7$: the arise of second- and third fundamental frequencies, f_2, f_3; (*o*) $M = 7$: limit torus; (*p*) $M = 8$: chaotic state; (*q*) $M = 8$: broadband continuous spectrum; (*r*) $M = 8$: chaotic attractor.

Re	M	Lyapunov exponent (λ)	Motion state
250	1	NA	steady
250	4	0.0073	periodic
250	5	0.014	period-doubling
250	6	0.0035	periodic
250	7	0.01	quasi-periodic
250	8	0.5705	chaotic

Table 4. Estimated dominant Lyapunov exponent and corresponding motion state of the system: $K_s = 2400$, $P_e = 1.95$. Here NA means not applicable.

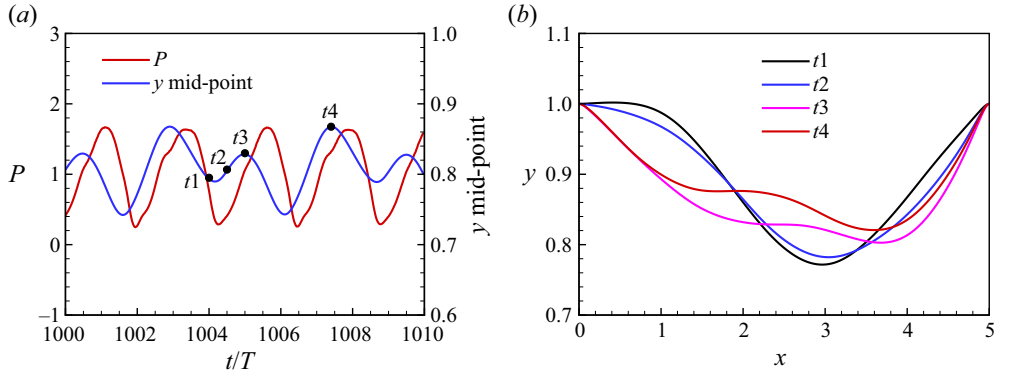

Figure 17. Travelling-wave flutter at $Re = 250$, $M = 5$, $P_e = 1.95$ and $K_s = 2400$: (*a*) the time histories of pressure and *y*-coordinate for the mid-point ($x = 2.5$ initially) on the upper elastic wall; (*b*) the spatial wave of the wall shapes at four different instants shown in (*a*). (*a*) The *p* and *y*-coordinate time histories, (*b*) wall shapes.

shown in figure 16(*c*). When M increases to 4, the wall motion is periodic (see figure 16*d*) with a fundamental frequency f_1 and its harmonics (i.e. $2f_1$, $3f_1$ etc) (see figure 16*e*). This is supported by the limit cycle in figure 16(*f*). When the mass ratio increases to $M = 5$, the system settles into a period-doubling state, which is confirmed by the appearance of subharmonic frequencies $0.5f_1$ and $1.5f_1$ in figure 16(*h*) and multiple limit cycles in figure 16(*i*). Figure 16(*g*) shows the corresponding motion state. At $M = 6$, the system experiences a period-1 limit cycle oscillation, as demonstrated by the periodic oscillations in figure 16(*j*), the PSD in figure 16(*k*) and a single limit cycle in figure 16(*l*). The system then enters a quasi-periodic motion at $M = 7$ as evidenced by the quasi-periodic wave shapes in figure 16(*m*), the PSD in figure 16(*n*) and the limit torus in figure 16(*o*). At $M = 8$, the broadband continuous spectrum in figure 16(*q*) and the chaotic attractor in figure 16(*r*) indicate that the system enters a chaotic motion. The estimated dominant Lyapunov exponents λ for these cases listed in table 4, support the identification of chaotic motion at $M = 8$ ($\lambda = 0.5705$ ($\sim$ of order 10^{-1})). Figure 16(*p*) shows that the corresponding chaotic motion involves non-repetitive irregular oscillations, which is quite different from the chaotic oscillations observed in figures 10(*j*) and 10(*s*) where the dynamic behaviours of the elastic walls feature small noise-like fluctuations.

The changes in behaviour with the increase of mass ratio are now explored by analysing the vortex structures shown in figure 18. Compared with the vortex structure in figure 11, the vortices in figure 18 are more apparent in the collapsible section of the channel

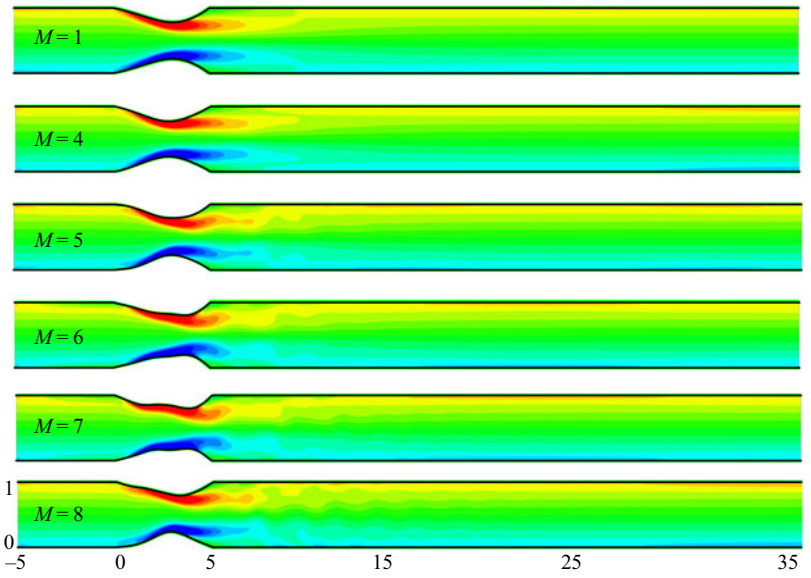

Figure 18. Instantaneous vorticity contours under different mass ratios at $t/T = 100$ with $Re = 250$, $K_s = 2400$ and $P_e = 1.95$. The vorticity ranges from -10 (blue) to 10 (red). Note: the aspect ratio (length/width) is set to 0.3 for an overview of the whole flow field. Animations of the vorticity contours for $M = 5$–8 are provided in supplementary movies 6 to 9.

compared with other regions. This difference is caused by the effects of Reynolds number. In figure 11 the Reynolds number for most cases are $Re \geq 500$, which causes a longer jet flow between the recirculation zones. Therefore, the vortices are less apparent in the collapsible section of the channel. As for the vortices in figure 18, a shorter jet flow is formed due to the low Reynolds number ($Re = 250$), leading to more apparent vortices in the collapsible section. At $Re = 250$, a negative transmural pressure causes the channel walls to indent inward. The relatively weak wall inertia at $M = 1$ enables the system to be steady with the formation of a stable jet flow. As the mass ratio increases to $M = 4$, the relatively heavy elastic walls periodically produce a jet flow, independent of the generation of vorticity waves downstream. This result indicates that the periodic oscillations of the elastic walls can be induced by increasing the wall inertia. The flow and wall shapes are still symmetric, indicating that symmetry breaking is not necessary for the onset of self-excited oscillations.

The effect of wall inertia becomes more evident at $M = 5$ with a pair of small vortices shedding downstream of the elastic walls. Due to the relatively strong diffusion of vortices at $Re = 250$, these vortices dissipate quickly. Figure 17(a) shows the time histories of pressure and y-coordinate for the mid-point on the upper elastic wall. The oscillations of the wall y-coordinate and wall pressure are slightly out of phase, indicating that energy has been irreversibly transferred to the elastic walls, leading to flutter of the walls. Figure 17(b) shows the spatial wave of the wall shapes at four instants shown in figure 17(a). The wall has one wave at $t1$ and $t2$, moving to two waves at $t3$ and $t4$ which implies that travelling-wave flutter is formed at $M = 5$. The travelling-wave flutter has also been found by Luo & Pedley (1998) for a one-sided collapsible channel flow. The period-doubling oscillations at $M = 5$ are caused by the travelling-wave flutter along the elastic walls (see supplementary movie 6 for an animation of the vorticity contours). At $M = 6$, a period-1 limit cycle oscillation has been induced by the wall inertia. The flow is still symmetric until

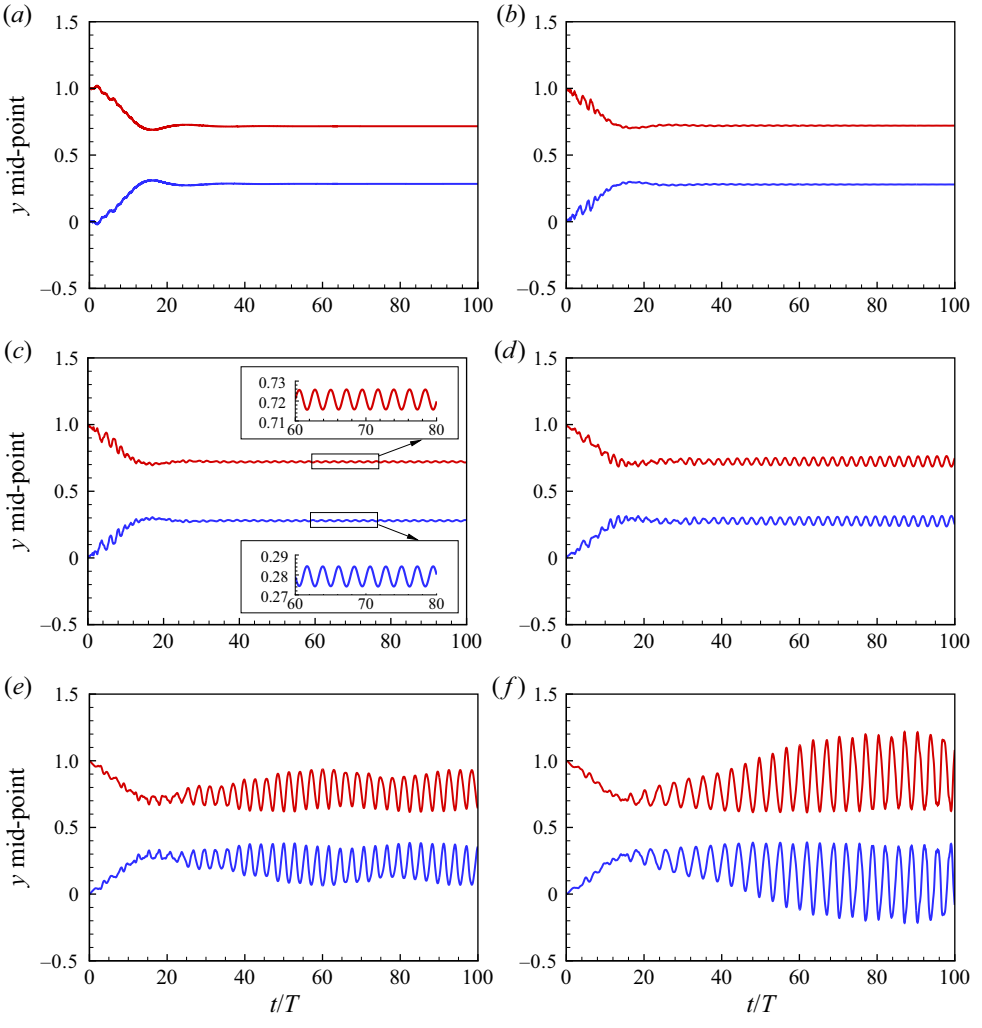

Figure 19. The time history of the y-coordinate for the mid-point ($x = 2.5$ initially) on the elastic walls for different mass ratios M with $Re = 500$, $K_s = 2400$, $P_e = 1.95$. The red line and blue line represent the upper and lower elastic wall, respectively. Plot parameters: (*a*) $M = 0.3$; (*b*) $M = 1$; (*c*) $M = 2$; (*d*) $M = 5$; (*e*) $M = 10$; (*f*) $M = 20$.

the symmetry breaking of the collapsible channel walls at $M = 8$. The chaotic oscillations at $M = 8$ (heavy walls) are due to symmetry breaking coupled with the travelling-wave oscillation along the elastic walls induced by the wall elasticity (see supplementary movie 9 for an animation of the vorticity contours). This scenario shows some similarity to the aeroelastic flutter of a bridge. For fixed $Re = 250$ with varying M, the mass ratio is the major parameter that causes symmetry breaking of the collapsible channel flow. Therefore, the mass ratio controls the onset of chaos, which will arise once this parameter becomes sufficiently high. A similar observation was reported by Connell & Yue (2007) for a 2-D flapping flag in a uniform flow.

Here the effects of a wider range of mass ratios are examined: $M = 0.3$, 1, 2, 5, 10 and 20 while the other non-dimensional governing parameters are fixed as follows: $Re = 500$, $K_s = 2400$ and $P_e = 1.95$. Figure 19 shows the time history of the y-coordinate

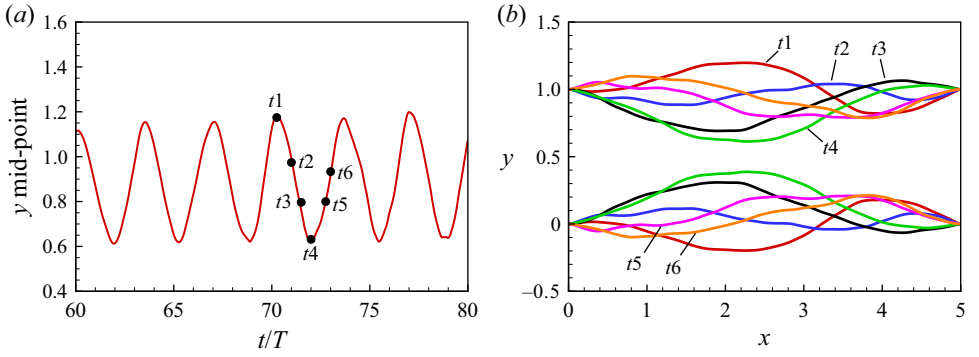

Figure 20. The y-coordinate time history for the mid-point ($x = 2.5$ initially) on the upper elastic wall (a) and the wall shapes (b) corresponding to the six instants shown in (a) for $M = 20$ with $Re = 500$, $K_s = 2400$, $P_e = 1.95$. (a) The y-coordinate time history. (b) Wall shapes.

of the mid-point of the elastic walls for different mass ratios. The oscillation amplitude of the elastic walls increases with the mass ratio M, with solutions that are steady for $M \leq 0.3$ (see figure 19(a), results of $M = 0.1$ and $M = 0.2$ not shown here). For $M = 1$, as shown in figure 19(b), the startup transient oscillation decays with time and the system reaches steady state at $t/T = 80$. When M is relatively small (e.g. $M \leq 2$), the oscillation amplitude is less than 0.01 (see figure 19c) but increases significantly for $M \geq 10$, as shown in figures 19(d) and 19(e), changing from small-amplitude mode at $M = 5$ to large-amplitude mode at $M = 10$. These results indicate that the self-excited oscillations of the elastic walls are closely related to the mass ratio of the wall.

Figure 19(f) shows an interesting oscillation mode at $M = 20$. Following the collapse of the elastic walls initially (from $t/T = 0$ to $t/T = 17$), the oscillation grows and settles into large amplitude. We examine one specific cycle in figures 20 and 21. Figure 20(a) shows the time history of the y-coordinate and figure 20(b) shows the corresponding wall shapes at six instants, as indicated in figure 20(a). It is seen from figure 20(b) that the deformations of the two elastic walls are always symmetric at $t1$ to $t6$. The walls bulge out strongly upstream at $t1$ then bounce back to a strongly collapsed state at $t4$.

In figure 21 the corresponding vorticity contours clearly show the vortex pair evolution, migration and dissipation process. The vortices are always symmetric even at this high wall inertia ($M = 20$). More specifically, a pair of vortices $p1$ is shed downstream of the elastic walls at $t1$ and is convected downstream accompanied with the collapse of the walls. A new vortex pair $p2$ is generated at $t2$ and is convected downstream with the further collapse of the elastic walls at $t3$. At $t4$ when the elastic walls reach to their most collapsed state, a strong central jet emerges and entrains the surrounding fluid including the vortices. After reopening of the collapsed channel, the former vortex pairs (i.e. $p1$ and $p2$) are convected further downstream ($t5$) and a new vortex pair $p3$ is shed again beyond the throat ($t6$). Such a fluid flow is different from the jet produced in a nozzle and shows some similarity to the jet propulsion of a cephalopod under water (Luo *et al.* 2020).

4.3. *Effects of external pressure P_e at $Re = 500$*

Here the effects of external pressure P_e (= 1, 2, 3, 5, 8 and 10) exerted on the elastic walls are further investigated, while the other non-dimensional governing parameters are fixed at $Re = 500$, $K_s = 2400$ and $M = 1$.

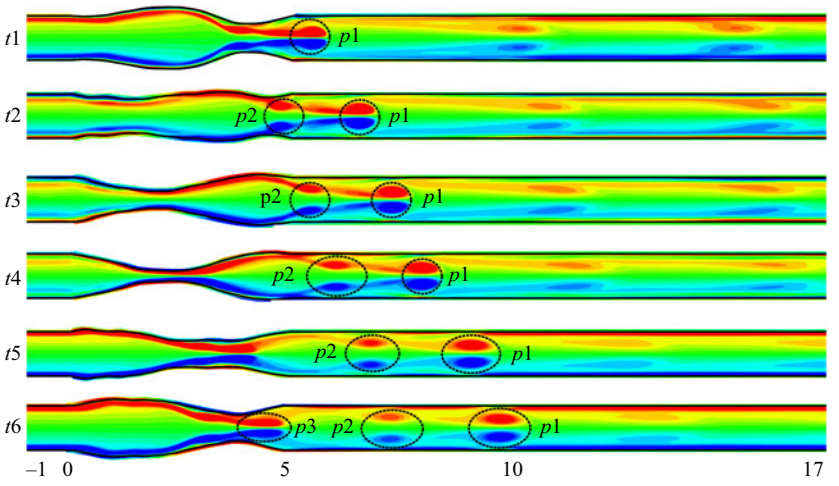

Figure 21. Instantaneous vorticity contours at six instants marked in figure 20(*a*) for $M = 20$, $Re = 500$, $K_s = 2400$, $P_e = 1.95$. The vorticity ranges from -7 (blue) to 7 (red).

Figure 22 shows the time history of the y-coordinate of the mid-point on the elastic walls. Overall, it is seen that self-excited oscillations occur under large external pressure (for $P_e \geq 5$, see figures 22*d*, 22*e* and 22*f*) and the oscillation amplitude increases with P_e. Specifically, as shown in figure 22(*a*) ($P_e = 1$), the walls reach a stable state immediately after collapse. For $P_e = 2$ and $P_e = 3$ (see figures 22*b* and 22*c*), the elastic walls experience small-amplitude oscillations, but the walls reach a steady state as the oscillations decay with time. At $P_e = 5$ and $P_e = 8$, small-amplitude (less than $0.01D$) self-excited oscillations are developed. As shown in figure 22(*f*), at $P_e = 10$, high-frequency small-amplitude self-excited oscillations are superimposed on low-frequency large-amplitude oscillations. These results indicate that P_e triggers the onset of self-excited oscillations and controls their amplitude.

We examine the special oscillation mode at $P_e = 10$. Figure 23 shows the time history of the y-coordinate of the mid-point at the upper elastic wall, and the vorticity contours at the seven instants marked in figure 23 are shown in figure 24. Figure 23 shows that the oscillations at $P_e = 10$ are highly irregular, which is in a chaotic motion state. It can be seen from figure 24 that the motions of the upper and lower elastic walls are asymmetric with complex vortex structures, in contrast to the symmetric vortex structures shown in figure 21. From $t1$ to $t4$, initially, the opposite elastic walls approach each other, reducing the cross-section area of the channel. The fluid reaches the maximum speed at the throat of the channel, reducing the pressure, which causes a further collapse of the channel until the channel is almost closed at $t5$. From $t1$ to $t4$, the vortices are convected downstream quickly until $t5$ when the vortices stop convecting downstream further until the channel reopens at $t6$. The kinetic energy of the upstream fluid is converted to a pressure increase that causes the channel to reopen at $t6$, and the cycle is repeated.

4.4. *Discussion*

A two-sided collapsible channel flow is numerically studied here. An IB-LBM FSI strategy is extended to model the FSI system. Compared with the conventional ALE, the IB-LBM FSI algorithm is simple because the Cartesian mesh is used and mesh movement is avoided. Further, the advantages of explicit calculation and the intrinsic parallel nature of LBM make the IB-LBM FSI solver much more efficient (up to 100 times) than the

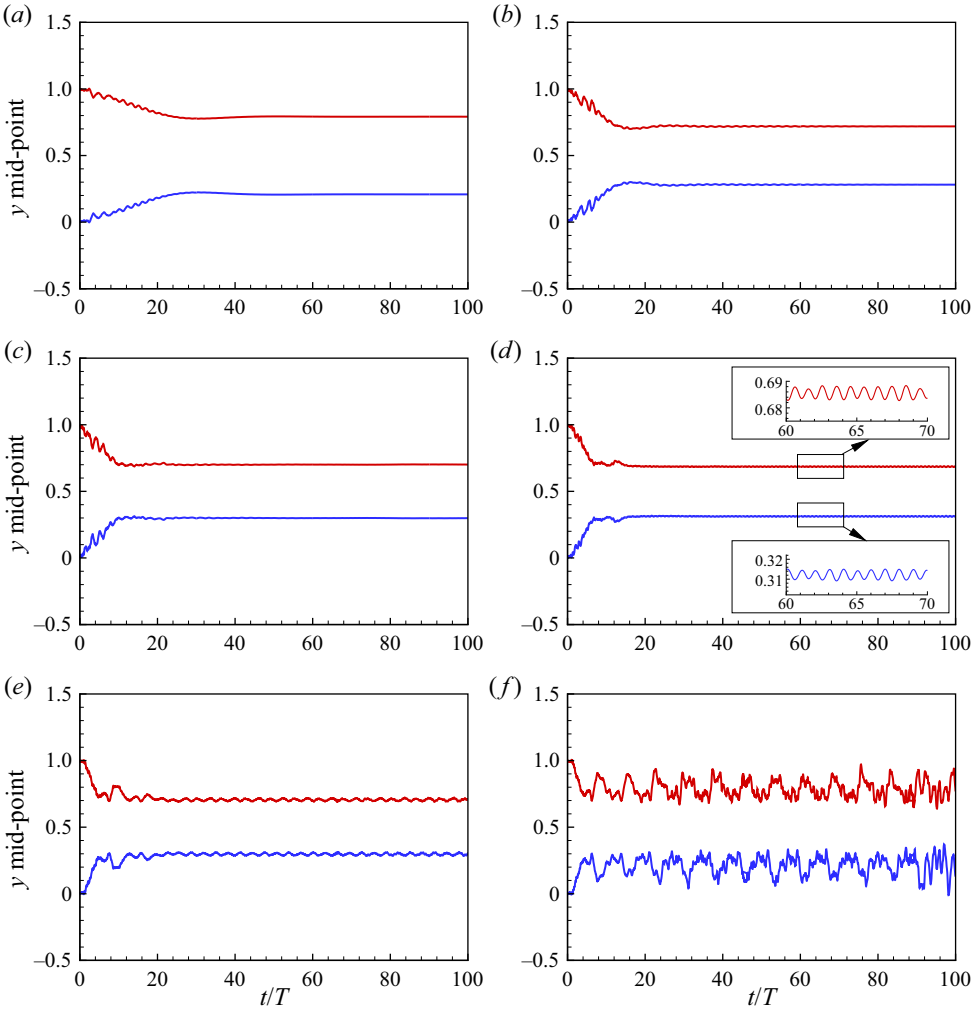

Figure 22. The time history of the y-coordinate of the mid-point ($x = 2.5$ initially) of the elastic walls under different external pressures P_e with $Re = 500$, $K_s = 2400$, $M = 1$. The red line and blue line represent the upper and lower elastic wall, respectively. Plot parameters: (*a*) $P_e = 1$; (*b*) $P_e = 2$; (*c*) $P_e = 3$; (*d*) $P_e = 5$; (*e*) $P_e = 8$; (*f*) $P_e = 10$.

conventional ALE FSI solver in terms of computation time (Luo *et al.* 2008). In addition, previously unexplored regions of the parameter space, such as high Reynolds number (*Re* up to 3000), high structure-to-fluid mass ratio (maximum $M = 100$) and high external pressure (maximum $P_e = 10$) are further examined here.

4.4.1. *The role of symmetry breaking*

Results here show that the symmetry breaking of the collapsible channel flow system may be induced by the increase of Reynolds number, wall inertia (mass ratio) and external pressure applied on the collapsible channel walls. Symmetry breaking is not a prerequisite for self-excited oscillations, but the symmetry breaking of the dynamic response of the elastic walls leads to the chaotic motion of this system.

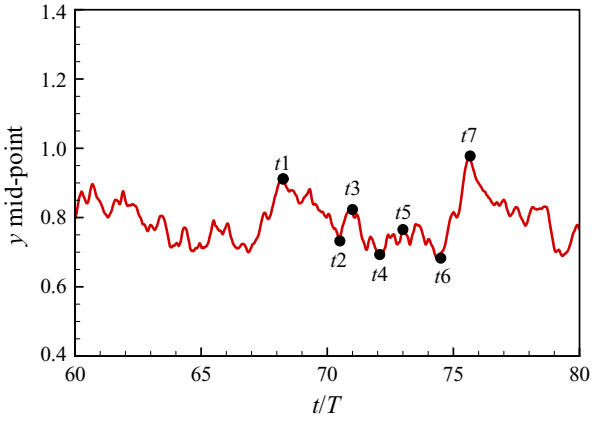

Figure 23. The time history of the y-coordinate for the mid-point ($x = 2.5$ initially) on the upper elastic wall with $M = 1$, $P_e = 10$, $Re = 500$ and $K_s = 2400$.

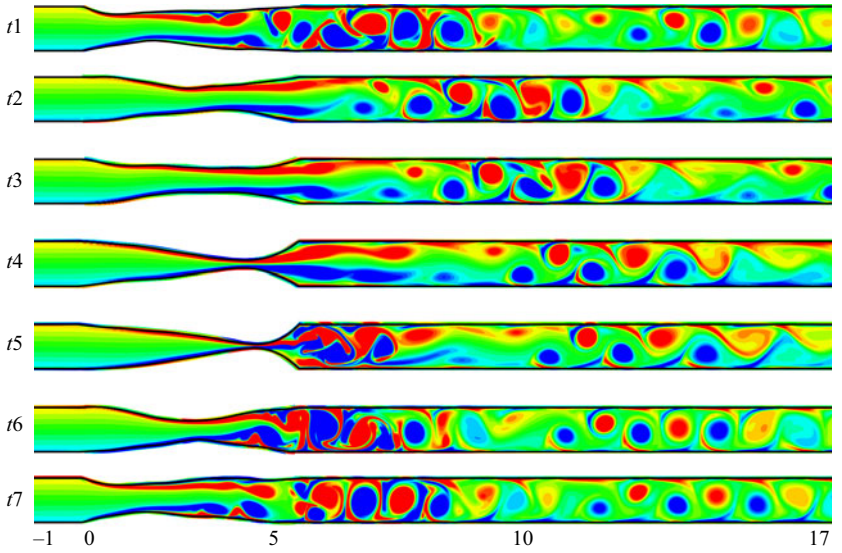

Figure 24. Instantaneous vorticity contours at seven instants during large-amplitude self-excited oscillations for $M = 1$, $P_e = 10$, $Re = 500$ and $K_s = 2400$. The vorticity ranges from -10 (blue) to 10 (red).

Firstly, at low mass ratio $M = 1$, the symmetry breaking arises at the Reynolds number of $Re = 320$ owing to a pitchfork bifurcation. The flow is steady both before and after the symmetry breaking bifurcation. A similar observation of such flow asymmetry has been reported by Kounanis & Mathioulakis (1999) in the experimental study of flow within a self-oscillating collapsible tube. They further reported that the flexible tube started oscillating when flow asymmetry occurred, while there are no oscillations in the collapsible walls here when flow asymmetry first appears. Kounanis & Mathioulakis (1999) pointed out that the symmetry breaking of the flow downstream of the collapsible segment may be a potential mechanism for the onset of self-excited oscillations. The different observations from this study are due to the much higher stretching stiffness and the negative transmural pressure (instead of a low and positive transmural pressure)

here as well as the geometric difference (i.e. two dimensional in our model and three dimensional in Kounanis & Mathioulakis 1999). The flow bifurcation investigated in § 4.1 shows that the occurrence of symmetry breaking of the jet flow at $Re = 320$ and $M = 1$ does not excite any oscillation of the elastic walls. In contrast, the collapsible channel flow system is still symmetric with periodic oscillations of the elastic walls at $Re = 250$ and $M = 2$ in § 4.2.2. Therefore, with regard to the role of symmetry breaking in the instability of a collapsible flow system, the different dynamic behaviours at $Re = 320$ for $M = 1$ and $Re = 250$ for $M = 2$ indicate that the symmetry breaking is not a prerequisite for the onset of self-excited oscillations.

Secondly, as shown in § 4.2.2, for $Re = 250$, the collapsible channel flow is symmetric for $M \leq 7$, and the symmetry breaking of the collapsible channel walls occurs at $M = 8$, where the system settles into a chaotic state. Finally, as shown in figures 22 and 23, for $M = 1$, the symmetry breaking occurs at $P_e = 10$ where the system settles into a chaotic state again. These observations indicate that the symmetry breaking induced by the wall inertia and the external pressure can lead the collapsible system into a chaotic state.

4.4.2. *Chaotic channel wall motions*

The existence of chaotic motion is confirmed by a positive dominant Lyapunov exponent ($\geq 10^{-2}$) and a chaotic attractor in the phase portrait of the y velocity displacement of the mid-point at the collapsible channel walls. Aperiodic oscillations were observed experimentally by Bertram *et al.* (1991) for $Re > 4400$ in a thick-walled silicone rubber tube. The presence of chaos cannot be certainly confirmed due to the limited time recordings made in their experiments. Results in § 4.2 show that chaos can occur over a wide range of Reynolds numbers (i.e. $100 \leq Re \leq 1000$), predominantly for high Reynolds numbers at low mass ratios (i.e. $Re \geq 500$ and $M \leq 4$); and for low Reynolds numbers with high mass ratios (i.e. $Re \leq 300$ and $M \geq 6$). Furthermore, in a general investigation of the routes to chaos for this system, two possibilities are found: the system reaches chaos via period-doubling or quasi-periodic bifurcations. The routes to chaos in the collapsible system have not been reported previously.

4.4.3. *Rich dynamic behaviours*

The dynamic behaviours of the collapsible system are qualitatively categorized into four major groups. The first group involves periodic oscillations of single fundamental frequency f_1. The second group involves period-doubling oscillations of one fundamental frequency f_1 and its subharmonic frequencies $0.5f_1$ and $1.5f_1$. These period-doubling oscillations show two different wave shapes (e.g. figure 10*m* and 16*g*). The third group, as is shown in figure 10(*p*), involves quasi-periodic oscillations of three incommensurate frequencies (i.e. f_1, f_2 and f_3). The last group involves chaotic oscillations including small noise-like fluctuations (e.g. figures 10*j* and 10*s*) and non-repetitive irregular oscillations (e.g. figure 16*p*). Similar oscillation types were also observed by Bertram *et al.* (1990) in the experimental study of collapsed tubes, where the experimentally observed oscillation types were categorized into six major groups including highly nonlinear periodic oscillations of relatively low frequency with two groups of different wave shapes, intermediate-frequency oscillations (nonlinear periodic oscillations at two or three times the frequency), high-frequency oscillations, smaller non-repetitive noise-like fluctuations and very-high-frequency oscillations. Irregular oscillations were also observed in their experiments as a genuine part of the dynamical behaviours of the collapsible system rather than due to any lack of control of experimental conditions.

4.4.4. *Physical mechanisms responsible for the onset of self-excited oscillations*

A wide range of the controlled parameters of the collapsible channel flows are investigated in this study ($100 \leq Re \leq 3000$, $0.3 \leq M \leq 100$ and $1 \leq P_e \leq 10$), and rich dynamic behaviours of the collapsible system are observed. The physical mechanisms responsible for the onset of these different oscillations are different, depending on the controlled parameters, and are summarized as follows.

(i) Unbalanced transmural pressure. In the investigation of the effects of Reynolds number shown in § 4.2.1, for $Re \leq 500$, $M \leq 1$, $P_e = 1.95$ and $K_s = 2400$, there is no vortex shedding downstream of the elastic walls and the stability of the collapsible channel walls are mainly determined by the transmural pressure. Under these parameter conditions, the viscosity is strong enough to damp out any small disturbances caused by wall inertia. The only unstable source, take $Re = 200$ as an example, comes from the unbalanced transmural pressure (positive upstream and negative downstream) along the elastic walls that causes self-excited oscillations. Either positive transmural pressure ($Re = 100$) or negative transmural pressure ($250 \leq Re \leq 500$) along the elastic walls can produce a steady state. Luo *et al.* (2008) demonstrated that the transmural pressure could affect the stability of the collapsible system through its interaction with the wall curvature, which supports our findings here.

(ii) Shear layer instabilities. As the Reynolds number increases, it is found that the generation and shedding of vortices play a major role in the stability of the collapsible system. The shedding of vortices downstream of the throat feeds back perturbations on the elastic walls. For $M \leq 1$, the instabilities in the wall motion for $550 \leq Re \leq 3000$ are mainly due to shear layer instabilities. Luo & Pedley (1996) firstly showed in a coupled FSI of a one-sided collapsible channel that the oscillations are a consequence of the generation of vorticity waves downstream. The effects of Re in § 4.2.1 reveal that the vortex shedding downstream of the throat are responsible for the onset of self-excited oscillations. Furthermore, the period-doubling, quasi-periodic and chaotic oscillations are closely associated with vortex pairing and merging of adjacent vortices, and the interactions between vortices on the upper and lower walls.

(iii) Wall elasticity at large mass ratios. For the onset of chaotic oscillations at $Re = 250$ and $M = 8$ in § 4.2.2, travelling-wave flutter along the elastic walls induced by the wall elasticity causes the symmetry breaking that further triggers chaotic oscillations. For high Reynolds numbers at high mass ratios, as shown in figure 14, the travelling-wave flutter induced by the wall elasticity at high mass ratios (e.g. $M = 10$) increases the oscillation amplitude approximately by a factor of five (e.g. from $0.02D$ at $M = 1$ and $Re = 2000$ to $0.1D$ at $M = 10$ and $Re = 2000$). The numerical study of the effects of wall inertia on a one-sided collapsible channel flow of Luo & Pedley (1998) is the first study where collapse and flutter were examined together. They focused on low mass ratios ($M \leq 1$) as otherwise the amplitude of the oscillations became too large for the mesh generator to manage. As was observed by Luo & Pedley (1998), the flutter observed here is not a consequence of the generation of vorticity waves downstream. The flutter found in Luo & Pedley (1998) was caused by a phase difference between the wall pressure and wall displacement, which enables the fluid to transfer energy continuously to the wall. The flutter observed in this study shows similarity to the high-frequency oscillations in the experimental observations of Bertram (1986) and Bertram *et al.* (1990), stemming from wall mass.

(iv) Heavy wall. The wall inertia can be neglected when the structure-to-fluid mass ratio is very small (e.g. the fluid is water), however, it cannot be neglected if the fluid is air (e.g. in the context of vocal fold oscillations during phonation). Luo & Pedley (1998) reported that the inclusion of wall inertia would introduce an additional high-frequency flutter mode of a one-sided collapsible channel wall. For the effects of mass ratio, as shown in figure 19, it is found that the self-excited oscillations can be triggered by the wall inertia, and the amplitude of oscillations increases with the wall inertia.

(v) High external pressure P_e. The onset of self-excited oscillations can also be triggered by P_e, and the oscillating amplitude increases with P_e. A similar observation was reported by Tang *et al.* (2015) for a one-sided collapsible channel flow. At $P_e = 10$, the elastic walls experience high-frequency small-amplitude self-excited oscillations superimposed on low-frequency large-amplitude oscillations, which is a chaotic motion state. The vorticity contours in figure 24 show the near occlusion and reopening process of the collapsible system at $P_e = 10$, which is quite similar to the collapse of brachial arteries during blood-pressure measurements (Bertram *et al.* 1989).

5. Conclusions

In this paper the nonlinear dynamics of a two-sided collapsible channel flow has been investigated by using an immersed IB-LBM. The transition routes from steady to chaotic motion of the collapsible system have been studied using nonlinear dynamic analysis. The role of symmetry breaking in the onset of self-excited oscillations is highlighted, and nonlinear and rich dynamic behaviours of this collapsible system are newly observed. The physical mechanisms responsible for the onset of self-excited oscillations of this collapsible system have been explored.

Firstly, the system may experience a supercritical Hopf bifurcation to a period-1 limit cycle oscillation. The existence of chaotic motion of the system is confirmed by a positive dominant Lyapunov exponent and a chaotic attractor in the phase portrait of the velocity displacement of the mid-point of the collapsible channel wall. The system has been shown to reach chaos via period-doubling and quasi-periodic bifurcations. Secondly, for the exploration of physical mechanisms responsible for the onset of self-excited oscillations, it has been found that the symmetry breaking of the collapsible channel flow system may be induced by increasing the Reynolds number, wall inertia and external pressure. Symmetry breaking is not a prerequisite for the onset of self-excited oscillations, but the symmetry breaking of the dynamic response of the collapsible channel walls leads to the chaotic motion of the collapsible walls. The unbalanced transmural pressure and the shear layer instabilities in the vorticity waves are responsible for the onset of the self-excited oscillations of this collapsible system. In addition, the period-doubling, quasi-periodic and chaotic oscillations are closely associated with vortex pairing and merging of adjacent vortices, and the interactions between the upper and lower vorticity rows. For a heavy wall, travelling-wave flutter along the elastic walls induced by the wall mass causes the symmetry breaking of the elastic walls that further triggers the chaotic oscillations. Finally, it has been found that large-amplitude self-excited oscillations of the collapsible system can be induced by high mass ratio and external pressure.

Supplementary movies. Movie 1. $Re = 200$, $M = 1$, $K_s = 2400$ and $P_e = 1.95$. Movie 2. $Re = 550$, $M = 1$, $K_s = 2400$ and $P_e = 1.95$. Movie 3. $Re = 600$, $M = 1$, $K_s = 2400$ and $P_e = 1.95$. Movie 4. $Re = 650$, $M = 1$, $K_s = 2400$ and $P_e = 1.95$. Movie 5. $Re = 800$, $M = 1$, $K_s = 2400$ and $P_e = 1.95$. Movie 6. $Re = 250$, $M = 5$,

$K_s = 2400$ and $P_e = 1.95$. Movie 7. $Re = 250$, $M = 6$, $K_s = 2400$ and $P_e = 1.95$. Movie 8. $Re = 250$, $M = 7$, $K_s = 2400$ and $P_e = 1.95$. Movie 9. $Re = 250$, $M = 8$, $K_s = 2400$ and $P_e = 1.95$. Supplementary movies are available at https://doi.org/10.1017/jfm.2021.710.

Funding. Mr Q. Huang acknowledges the support of the University International Postgraduate Award by the University of New South Wales. Dr F.-B. Tian is the recipient of an Australian Research Council Discovery Early Career Researcher Award (project number DE160101098). The computation work of this research was partially performed on the National Computational Infrastructure (NCI) supported by the Australian Government.

Declaration of interests. The authors report no conflict of interest.

Author ORCIDs.
Qiuxiang Huang https://orcid.org/0000-0002-9882-4942;
Fang-Bao Tian https://orcid.org/0000-0002-1247-6896;
John Young https://orcid.org/0000-0002-8671-990X;
Joseph C.S. Lai https://orcid.org/0000-0002-8946-9993.

References

Aidun, C.K. & Clausen, J.R. 2010 Lattice-Boltzmann method for complex flows. *Annu. Rev. Fluid Mech.* **42**, 439–472.

Battaglia, F., Tavener, S.J., Kulkarni, A.K. & Merkle, C.L. 1997 Bifurcation of low Reynolds number flows in symmetric channels. *AIAA J.* **35**, 99–105.

Bertram, C.D. 1986 Unstable equilibrium behaviour in collapsible tubes. *J. Biomech.* **19**, 61–69.

Bertram, C.D., Raymond, C.J. & Butcher, K.S.A. 1989 Oscillations in a collapsed-tube analog of the brachial artery under a sphygmomanometer cuff. *Trans. ASME J. Biomech. Engng* **111**, 185–191.

Bertram, C.D., Raymond, C.J. & Pedley, T.J. 1990 Mapping of instabilities for flow through collapsed tubes of differing length. *J. Fluids Struct.* **4**, 125–153.

Bertram, C.D., Raymond, C.J. & Pedley, T.J. 1991 Application of nonlinear dynamics concepts to the analysis of self-excited oscillations of a collapsible tube conveying a fluid. *J. Fluids Struct.* **5**, 391–426.

Bertram, C.D. & Tscherry, J. 2006 The onset of flow-rate limitation and flow-induced oscillations in collapsible tubes. *J. Fluids Struct.* **22**, 1029–1045.

Bluestein, D., Gutierrez, C., Londono, M. & Schoephoerster, R.T 1999 Vortex shedding in steady flow through a model of an arterial stenosis and its relevance to mural platelet deposition. *Ann. Biomed. Engng* **27**, 763–773.

Borazjani, I., Ge, L. & Sotiropoulos, F. 2008 Curvilinear immersed boundary method for simulating fluid structure interaction with complex 3D rigid bodies. *J. Comput. Phys.* **227**, 7587–7620.

Cai, Z.X. & Luo, X.Y. 2003 A fluid-beam model for flow in a collapsible channel. *J. Fluids Struct.* **17**, 125–146.

Cancelli, C. & Pedley, T.J. 1985 A separated-flow model for collapsible-tube oscillations. *J. Fluid Mech.* **157**, 375–404.

Chen, S. & Doolen, G.D. 1998 Lattice Boltzmann method for fluid flows. *Annu. Rev. Fluid Mech.* **30**, 329–64.

Connell, B.S.H. & Yue, D.K.P. 2007 Flapping dynamics of a flag in a uniform stream. *J. Fluid Mech.* **581**, 33–67.

Dai, G., Gertler, J.P. & Kamm, R.D. 1999 The effects of external compression on venous blood flow and tissue deformation in the lower leg. *Trans. ASME J. Biomech. Engng* **121**, 557–564.

Davies, C. & Carpenter, P.W. 1997*a* Instabilities in a plane channel flow between compliant walls. *J. Fluid Mech.* **352**, 205–243.

Davies, C. & Carpenter, P.W. 1997*b* Numerical simulation of the evolution of Tollmien-Schlichting waves over finite compliant panels. *J. Fluid Mech.* **335**, 361–392.

Favier, J., Revell, A. & Pinelli, A. 2014 A lattice Boltzmann-immersed boundary method to simulate the fluid interaction with moving and slender flexible objects. *J. Comput. Phys.* **261**, 145–161.

Feigenbaum, M.J. 1978 Quantitative universality for a class of nonlinear transformations. *J. Stat. Phys.* **19**, 25–52.

Feigenbaum, M.J. 1979 The universal metric properties of nonlinear transformations. *J. Stat. Phys.* **21**, 669–706.

FENG, L.Y., GAO, H., GRIFFITH, B., NIEDERER, S. & LUO, X.Y. 2019 Analysis of a coupled fluid–structure interaction model of the left atrium and mitral valve. *Intl J. Numer. Meth. Biomed. Engng* **35**, e3254.

FENG, Z.G. & MICHAELIDES, E.E. 2004 The immersed boundary-lattice Boltzmann method for solving fluid-particles interaction problems. *J. Comput. Phys.* **195**, 602–628.

GILMANOV, A., LE, T. & SOTIROPOULOS, F. 2015 A numerical approach for simulating fluid structure interaction of flexible thin shells undergoing arbitrarily large deformations in complex domains. *J. Comput. Phys.* **300**, 814–843.

GOZA, A., COLONIUS, T. & SADER, J.E. 2018 Global modes and nonlinear analysis of inverted-flag flapping. *J. Fluid Mech.* **857**, 312–344.

GRIFFITH, B.E. & PATANKAR, N.A. 2020 Immersed methods for fluid–structure interaction. *Annu. Rev. Fluid Mech.* **52**, 421–448.

GROTBERG, J.B. & JENSEN, O.E. 2004 Biofluid mechanics in flexible tubes. *Annu. Rev. Fluid Mech.* **36**, 121–147.

GUIOT, G., PIANTA, P.G., CANCELLI, C. & PEDLEY, T.J. 1990 Prediction of coronary blood flow with a numerical based on collapsible tube dynamics model. *Am. J. Physiol. Heart Circ. Physiol.* **258**, H1606–H1614.

GUO, Z.-L., ZHENG, C.-G. & SHI, B.-C. 2002 Non-equilibrium extrapolation method for velocity and pressure boundary conditions in the lattice Boltzmann method. *Chin. Phys.* **11**, 366–374.

HAZEL, A.L. & HEIL, M. 2003 Steady finite-Reynolds-number flows in three-dimensional collapsible tubes. *J. Fluid Mech.* **486**, 79–103.

HEIL, M. & BOYLE, J. 2010 Self-excited oscillations in three-dimensional collapsible tubes: simulating their onset and large-amplitude oscillations. *J. Fluid Mech.* **652**, 405–426.

HEIL, M. & HAZEL, A.L. 2011 Fluid–structure interaction in internal physiological flows. *Annu. Rev. Fluid Mech.* **43**, 141–162.

HUA, R., ZHU, L. & LU, X.-Y. 2014 Dynamics of fluid flow over a circular flexible plate. *J. Fluid Mech.* **759**, 56–72.

HUANG, W.-X., SHIN, S.J. & SUNG, H.J. 2007 Simulation of flexible filaments in a uniform flow by the immersed boundary method. *J. Comput. Phys.* **226**, 2206–2228.

HUANG, W.-X. & TIAN, F.-B. 2019 Recent trends and progress in the immersed boundary method. *Proc. Inst. Mech. Engng C* **233**, 7617–7636.

HUSSAIN, A.K.M.F. 1986 Coherent structures and turbulence. *J. Fluid Mech.* **173**, 303–356.

JENSEN, O.E. 1990 Instabilities of flow in a collapsed tube. *J. Fluid Mech.* **220**, 623–659.

JENSEN, O.E. 1992 Chaotic oscillations in a simple collapsible-tube model. *Trans. ASME J. Biomech. Engng* **114**, 55–59.

JENSEN, O.E. & HEIL, M. 2003 High-frequency self-excited oscillations in a collapsible-channel flow. *J. Fluid Mech.* **481**, 235–268.

KANG, S.K. & HASSAN, Y.A. 2011 A comparative study of direct-forcing immersed boundary-lattice Boltzmann methods for stationary complex boundaries. *Intl J. Numer. Meth. Fluids* **66**, 1132–1158.

KHEIRI, M. 2020 Nonlinear dynamics of imperfectly-supported pipes conveying fluid. *J. Fluids Struct.* **93**, 102850.

KOUNANIS, K. & MATHIOULAKIS, D.S. 1999 Experimental flow study within a self oscillating collapsible tube. *J. Fluids Struct.* **13**, 61–73.

KRÜGER, T., KUSUMAATMAJA, H., KUZMIN, A., SHARDT, O., SILVA, G. & VIGGEN, E.M. 2017 *The Lattice Boltzmann Method*. Springer International Publishing.

KRÜGER, T., VARNIK, F. & RAABE, D. 2011 Efficient and accurate simulations of deformable particles immersed in a fluid using a combined immersed boundary lattice Boltzmann finite element method. *Comput. Maths Applics.* **61**, 3485–3505.

KU, D.N. 1997 Blood flow in arteries. *Annu. Rev. Fluid Mech.* **29**, 399–434.

LALLEMAND, P. & LUO, L.-S. 2000 Theory of the lattice Boltzmann method: dispersion, dissipation, isotropy, Galilean invariance, and stability. *Phys. Rev.* E **61**, 6546–6562.

LIU, H.F., LUO, X.Y. & CAI, Z.X. 2012 Stability and energy budget of pressure-driven collapsible channel flows. *J. Fluid Mech.* **705**, 348–370.

LIU, H.F., LUO, X.Y., CAI, Z.X. & PEDLEY, T.J. 2009 Sensitivity of unsteady collapsible channel flows to modelling assumptions. *Commun. Numer. Meth. Engng* **25**, 483–504.

LUCEY, A.D. & CARPENTER, P.W. 1992 A numerical simulation of the interaction of a compliant wall and inviscid flow. *J. Fluid Mech.* **234**, 121–146.

LUCEY, A.D. & CARPENTER, P.W. 1995 Boundary layer instability over compliant walls: comparison between theory and experiment. *Phys. Fluids* **7**, 2355–2363.

LUO, L.-S., LIAO, W., CHEN, X., PENG, Y. & ZHANG, W. 2011 Numerics of the lattice Boltzmann method: effects of collision models on the lattice Boltzmann simulations. *Phys. Rev.* E **83**, 1–24.

LUO, X.Y., CAI, Z.X., LI, W.G. & PEDLEY, T.J. 2008 The cascade structure of linear instability in collapsible channel flows. *J. Fluid Mech.* **600**, 45–76.

LUO, X.Y., CALDERHEAD, B., LIU, H.F. & LI, W.G. 2007 On the initial configurations of collapsible channel flow. *Comput. Struct.* **85**, 977–987.

LUO, X.Y. & PEDLEY, T.J. 1995 A numerical simulation of steady flow in a 2-D collapsible channel. *J. Fluids Struct.* **9**, 149–174.

LUO, X.Y. & PEDLEY, T.J. 1996 A numerical simulation of unsteady flow in a two-dimensional collapsible channel. *J. Fluid Mech.* **314**, 191–225.

LUO, X.Y. & PEDLEY, T.J. 1998 The effects of wall inertia on flow in a two-dimensional collapsible channel. *J. Fluid Mech.* **363**, 253–280.

LUO, Y., XIAO, Q., ZHU, Q. & PAN, G. 2020 Pulsed-jet propulsion of a squid-inspired swimmer at high Reynolds number. *Phys. Fluids* **32**, 111901.

MA, J.T., WANG, Z., YOUNG, J., LAI, J.C.S., SUI, Y. & TIAN, F.-B. 2020 An immersed boundary-lattice Boltzmann method for fluid–structure interaction problems involving viscoelastic fluids and complex geometries. *J. Comput. Phys.* **415**, 109487.

MANNEVILLE, P. & POMEAU, Y. 1980 Different ways to turbulence in dissipative dynamical systems. *Physica* D **1**, 219–226.

MARZO, A., LUO, X.Y. & BERTRAM, C.D. 2005 Three-dimensional collapse and steady flow in thick-walled flexible tubes. *J. Fluids Struct.* **20**, 817–835.

MIOZZI, M., QUERZOLI, G. & ROMANO, G.P. 1998 The investigation of an unstable convective flow using optical methods. *Phys. Fluids* **10**, 2995–3008.

MITTAL, R. & IACCARINO, G. 2005 Immersed boundary methods. *Annu. Rev. Fluid Mech.* **37**, 239–261.

NEWHOUSE, S., RUELLE, D. & TAKENS, F. 1978 Occurrence of strange axioma attractors near quasi periodic flows on T^m, $m \geq 3$. *Commun. Math. Phys.* **64**, 35–40.

OHBA, K, SKURAI, A. & OKA, J. 1997 Laser Doppler measurement of local flow field in collapsible tube during self-excited oscillation. *JSME Intl J.* **40**, 665–670.

OLIVEIRA, M.S.N., RODD, L.E., MCKINLEY, G.H. & ALVES, M.A. 2008 Simulations of extensional flow in microrheometric devices. *Microfluid Nanofluidics* **5**, 809.

PEDLEY, T.J. 1992 Longitudinal tension variation in collapsible channels: a new mechanism for the breakdown of steady flow. *Trans. ASME J. Biomech. Engng* **114**, 60–67.

PESKIN, C.S. 1972 Flow patterns around heart valves: a numerical method. *J. Comput. Phys.* **10**, 252–271.

PESKIN, C.S. 2002 The immersed boundary method. *Acta Numer.* **11**, 479–517.

ROCHA, G.N., POOLE, R.J. & OLIVEIRA, P.J. 2007 Bifurcation phenomena in viscoelastic flows through a symmetric 1:4 expansion. *J. Non-Newtonian Fluid* **141**, 1–17.

RUELLE, D. & TAKENS, F. 1971 On the nature of turbulence. *Commun. Math. Phys.* **20**, 167–192.

SHAPIRO, A.H. 1977 Steady flow in collapsible tubes. *Trans. ASME J. Biomech. Engng* **99**, 126–147.

SOBEY, I.J. & DRAZIN, P.G. 1986 Bifurcations of two-dimensional channel flows. *J. Fluid Mech.* **171**, 263–287.

SOTIROPOULOS, F. & YANG, X. 2014 Immersed boundary methods for simulating fluid–structure interaction. *Prog. Aerosp. Sci.* **65**, 1–21.

STEWART, P.S., HEIL, M., WATERS, S.L. & JENSEN, O.E. 2010 Sloshing and slamming oscillations in a collapsible channel flow. *J. Fluid Mech.* **662**, 288–319.

SUI, Y., CHEW, Y.T., ROY, P. & LOW, H.T. 2008 A hybrid method to study flow-induced deformation of three-dimensional capsules. *J. Comput. Phys.* **227**, 6351–6371.

TANG, C., ZHU, L., AKINGBA, G. & LU, X.-Y. 2015 Viscous flow past a collapsible channel as a model for self-excited oscillation of blood vessels. *J. Biomech.* **48**, 1922–1929.

TIAN, F.-B. 2014 FSI modeling with the DSD/SST method for the fluid and finite difference method for the structure. *Comput. Mech.* **54**, 581–589.

TIAN, F.-B., DAI, H., LUO, H.X., DOYLE, J.F. & ROUSSEAU, B. 2014 Fluid–structure interaction involving large deformations: 3D simulations and applications to biological systems. *J. Comput. Phys.* **258**, 451–469.

TIAN, F.-B., LUO, H., ZHU, L., LIAO, J.C. & LU, X.-Y. 2011*a* An efficient immersed boundary-lattice Boltzmann method for the hydrodynamic interaction of elastic filaments. *J. Comput. Phys.* **230**, 7266–7283.

TIAN, F.-B., LUO, H., ZHU, L. & LU, X.-Y. 2010 Interaction between a flexible filament and a downstream rigid body. *Phys. Rev.* E **82**, 026301.

TIAN, F.-B., LUO, H., ZHU, L. & LU, X.-Y. 2011*b* Coupling modes of three filaments in side-by-side arrangement. *Phys. Fluids* **23**, 111903.

TIAN, F.-B., WANG, Y., YOUNG, J. & LAI, J.C.S. 2015 An FSI solution technique based on the DSD/SST method and its applications. *Math. Models Meth. Appl. Sci.* **25**, 2257–2285.

TSIGKLIFIS, K. & LUCEY, A.D. 2017 Asymptotic stability and transient growth in pulsatile Poiseuille flow through a compliant channel. *J. Fluid Mech.* **820**, 370–399.

WANG, J.W., CHEW, Y.T. & LOW, H.T. 2009 Effects of downstream system on self-excited oscillations in collapsible tubes. *Commun. Numer. Meth. Engng* **25**, 429–445.

WANG, L., CURRAO, G.M.D., HAN, F., NEELY, A.J., YOUNG, J. & TIAN, F.-B. 2017 An immersed boundary method for fluid–structure interaction with compressible multiphase flows. *J. Comput. Phys.* **346**, 131–151.

WANG, L. & TIAN, F.-B. 2018 Heat transfer in non-Newtonian flows by a hybrid immersed boundary–lattice Boltzmann and finite difference method. *Appl. Sci.* **8**, 559.

WILLIAMS, H.A.R., FAUCI, L.J. & GAVER III, D.P. 2009 Evaluation of interfacial fluid dynamical stresses. *Discrete Continuous Dyn. Syst.* **11**, 519–540.

WOLF, A. 2021 Wolf lyapunov exponent estimation from a time series. MATLAB Central File Exchange. Retrieved June 6, 2021, https://www.mathworks.com/matlabcentral/fileexchange/48084-wolf-lyapunov-exponent-estimation-from-a-time-series.

WOLF, A., SWIFT, J.B., SWINNEY, H.L. & VASTANO, J.A. 1985 Determining Lyapunov exponents from a time series. *Physica* D **16**, 285–317.

XU, L.C., TIAN, F.-B., YOUNG, J. & LAI, J.C.S. 2018 A novel geometry-adaptive Cartesian grid based immersed boundary–lattice Boltzmann method for fluid–structure interactions at moderate and high Reynolds numbers. *J. Comput. Phys.* **375**, 22–56.

ZHANG, J., LIU, N.-S. & LU, X.-Y. 2009 Route to a chaotic state in fluid flow past an inclined flat plate. *Phys. Rev.* E **79**, 045306.

ZHANG, S., LUO, X.Y. & CAI, Z.X. 2018 Three-dimensional flows in a hyperelastic vessel under external pressure. *Biomech. Model. Mechanobiol.* **17**, 1187–1207.

ZHU, L., HE, G., WANG, S., MILLER, L., ZHANG, X., YOU, Q. & FANG, S. 2011 An immersed boundary method based on the lattice Boltzmann approach in three dimensions, with application. *Comput. Maths Applics.* **61**, 3506–3518.